RSC Advances

REVIEW

View Article Online
View Journal | View Issue

Cite this: *RSC Adv.*, 2025, **15**, 13370

Resistive nanostructured $W_{18}O_{49}$ gas sensors: an overview

M. Hjiri, [a] I. Najeh,*[b] Fatemah M. Barakat[c] and G. Neri[d]

Received 18th February 2025
Accepted 10th April 2025

DOI: 10.1039/d5ra01197c

rsc.li/rsc-advances

The detection of toxic gases by resistive gas sensors, which are mainly fabricated using semiconducting metal oxides, is of importance from a safety point of view. These sensors have outstanding electrical and sensing properties as well as are inexpensive. $W_{18}O_{49}$ ($WO_{2.72}$), which is a non-stoichiometric tungsten oxide, possesses abundant oxygen vacancies, which are beneficial for the adsorption of oxygen gas molecules and act as sites for sensing reactions. Thus, through the rational design of $W_{18}O_{49}$-based gas sensors using strategies such as morphology engineering, doping, decoration, formation of composites or their combination, the fabrication of high-performance $W_{18}O_{49}$ gas sensors is feasible. Herein, we present the gas-sensing features of pristine $W_{18}O_{49}$, doped $W_{18}O_{49}$, decorated $W_{18}O_{49}$ and composite-based $W_{18}O_{49}$ sensors. Moreover, focusing on the sensing mechanism of $W_{18}O_{49}$ sensors, this review provides an in-depth understanding on the working principles of the sensing of toxic gases using $W_{18}O_{49}$.

1. Introduction to resistive gas sensors

Owing to the rapid industrialization and extensive emission of toxic and dangerous gases from automobiles, chemical plants, food industry, mines, *etc.*, air pollution is becoming one of the main causes of human death in most countries.[1] Air pollution is linked to COVID-19 severity and mortality[2] and causes dizziness, reduced oxygen content in the blood, difficulty in breathing, as well as cardiovascular and respiratory issues.[3]

Traditionally, the presence of toxic gases can be demonstrated by techniques such as gas and ion chromatography.[4,5] However, these methods have the disadvantage of being expensive, bulky and complicated, which makes their application difficult for real-time and low power consumption gas detection.[6] Thus, the development of sensitive and reliable devices to detect toxic and harmful gases is essential. Gas sensors are sensitive electrical devices that can detect the presence of surrounding gases *via* the generation of an electrical signal due to a change in one of their physical properties such as capacitance or resistance. Gas sensors should have merits over traditional detection methods, such as portability and small size, low power consumption, on-line response, ease of fabrication and low cost.[7] To date, various types of sensors such as piezo-resistive,[8] electrochemical,[9] catalytic combustion,[10] thermal conductivity,[11] infrared absorption[12] and resistive gas sensors[13] based on different materials and principles have been introduced. Each type of gas sensor has its own merits and drawbacks. Among them, resistive sensors are the most widely used owing to their high stability, good response, cost-effectiveness, simple operation, fast dynamics, and ease of fabrication.[14] However, high sensing temperature and weak selectivity are the main drawbacks of this type of sensors.[15,16]

There are two types of sensor configurations: planar and tubular.[1] In both cases, resistive gas sensors are fabricated *via* the deposition of a sensing layer over a substrate equipped with electrons. Generally, alumina and SiO_2-coated Si are used as the substrate, and electrodes are fabricated using Pt, Au, and Pd–Ag. Moreover, on the back side of a planar sensor, a microheater is attached to the substrate, which is used for heating the sensor to the desired temperature, whereas in the case of tubular sensors, a resistive nichrome wire within the tubular substrate is used for heating the sensor.[1] Fig. 1(a)–(c) display a schematic of a planar sensor.

Various factors such as chemical composition, surface area, morphology, structure, and number of active sites significantly affect the sensing characteristics of gas sensors.[17] Therefore, the choice of sensing material is very important to bring about a high performance sensor. For the realization of resistive gas sensors, semiconducting metal oxides such as SnO_2 and ZnO are extensively employed,[18] owing to their abundance and high stability and electron mobility.[19] However, they have a high sensing temperature and relatively weak selectivity, especially in pristine form, similar to most other semiconducting-based sensors.[20] In this regards, the development of metal oxide gas sensors using other materials such as non-stoichiometric

[a]*Department of Physics, College of Sciences, Imam Mohammad Ibn Saud Islamic University (IMSIU), Riyadh, 11623, Saudi Arabia*

[b]*Laboratory of Physics of Materials and Nanomaterials Applied at Environment (LaPhyMNE), Faculty of Sciences in Gabes, Gabes University, Gabes, Tunisia. E-mail: Imededdine.Najeh@gmail.com*

[c]*Physics and Astronomy Department, Faculty of Science, King Saud University, Riyadh, Saudi Arabia*

[d]*Department of Engineering, University of Messina, Messina, 98166, Italy*

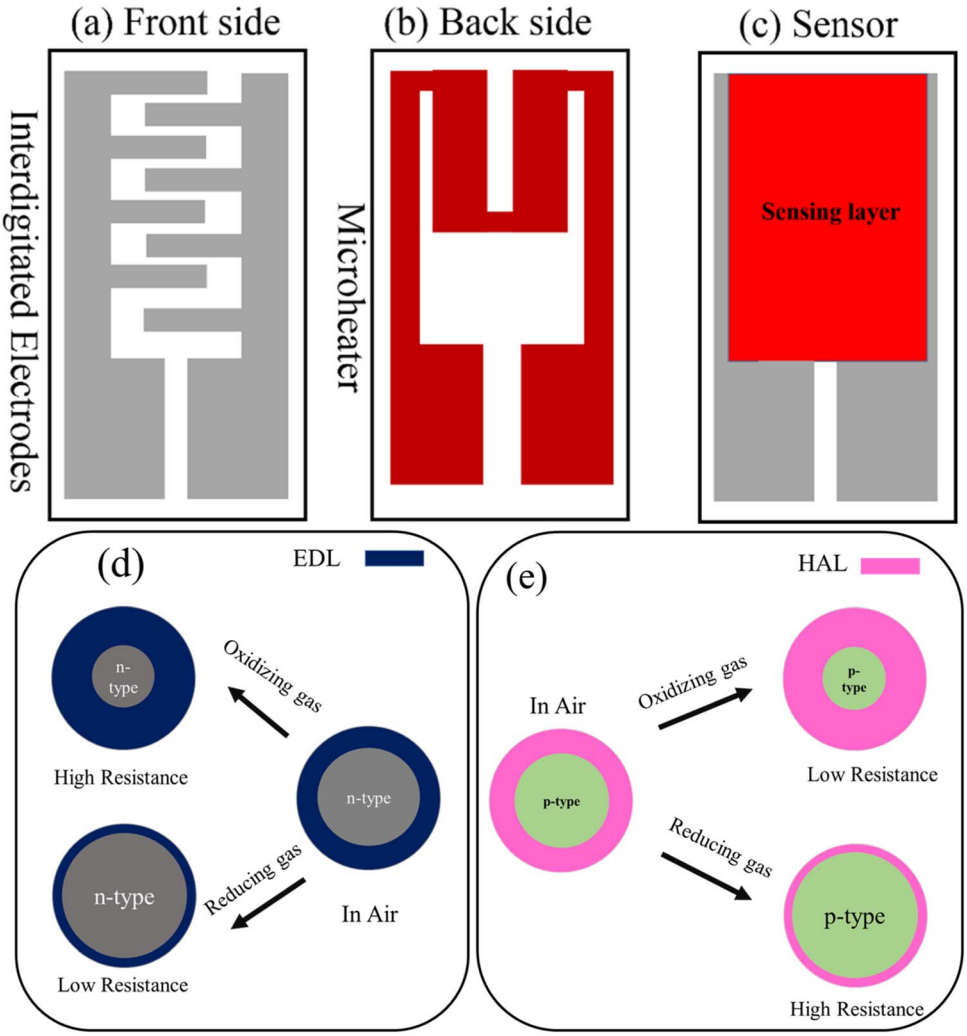

Fig. 1 Schematic of (a) the front side, (b) back side and (c) fabricated resistive gas sensor. General gas sensing mechanism of (d) n-type and (e) p-type gas sensors.

tungsten oxides (WO_{3-x}) can overcome some disadvantages associated with resistive gas sensors and may open some new doors in the exploration and design of high-performance gas sensors.

1.1 General gas sensing mechanism of resistive gas sensors

Resistance modulation is the key factor for the generation of a sensing signal in resistive gas sensors. Fig. 1(d) and (e) schematically illustrates the general gas sensing mechanism of n-type and p-type gas sensors, respectively. When a resistive gas sensor is exposed to fresh air, oxygen molecules with high electron affinity take electron from the sensor surface and become adsorbed on the surface. The abstraction of electrons by oxygen changes the resistance of the gas sensor relative to vacuum conditions, where there is no air. In the case of an n-type gas sensor, in which the main charge carriers are electrons, the abstraction of electrons causes the formation of an electron depletion layer, where the concentration of electrons is less than that in the inner parts, resulting in a high electrical resistance in air. In contrast, in a p-type gas sensor, the abstraction of electrons causes the formation of a hole accumulation layer (HAL), where the concentration of holes is much higher than that in the core region, resulting in a decrease in electrical resistance in air. When an n-type gas sensor is exposed to a reducing gas, electrons are released on the sensor surface, resulting in a decrease in the thickness of the EDL, which decreases the electrical resistance. However, in an oxidizing gas, further abstraction of electrons causes an increase in the thickness of the EDL, resulting in an increase in the sensor resistance. In the case of p-type gas sensors, the trends of resistance change are inverse, where the resistance increases and decreases in the presence of reducing and oxidizing gases, respectively.[21–23]

2. $W_{18}O_{49}$: an introduction

Tangiest oxide (WO_3) is a semiconductor with unique electrical properties and multifunctional applications.[24] Besides stoichiometric WO_3, non-stoichiometric WO_{3-x}, including $WO_{2.72}$

($W_{18}O_{49}$),[25] $WO_{2.8}$ (W_5O_{14})[26] and $WO_{2.9}$ ($W_{20}O_{58}$),[27] with abundant oxygen vacancies, is becoming an attractive candidate for the development of gas sensors owing to their abundance, low cost, nontoxicity, suitable band gap and high chemical stability.[28] In WO_{3-x}, the presence of oxygen vacancies results in the formation of shallow donors, increasing the number of adsorption sites and the electrical conductivity.[29] In particular, owing to the high conductivity[30] and abundant oxygen vacancies in $W_{18}O_{49}$ ($WO_{2.72}$), it has attracted significant attention compared to other WO_{3-x} materials.[31,32] In addition to gas sensors,[33–38] $W_{18}O_{49}$ has applications in energy storage,[39] medicine,[40] supercapacitors,[41] sonodynamic therapy,[42] and photocatalysts.[43]

Bhavani *et al.*,[24] Yan *et al.*,[39] and Zhou *et al.*[44] discussed the use of $W_{18}O_{49}$-based materials for energy and environmental use, energy storage conversion and photocatalysts, respectively. Although there are many reviews in the field of semiconductor gas sensors,[1,35,45,46] a review on $W_{18}O_{49}$ as a gas sensor is lacking. Inspired by this lack of review papers related to the gas sensing features of $W_{18}O_{49}$, herein, we discuss the sensing properties and mechanisms of pristine, doped and composite $W_{18}O_{49}$-based gas sensors.

$W_{18}O_{49}$ has the most reduced form among the WO_{3-x} oxides.[28] The crystal structure of $W_{18}O_{49}$ as a sub-stoichiometric type of WO_3 is formed by crystallographic shearing based on WO_3. WO_3 has a perovskite structure (ABO_3), in which the "A" site is missing.[31] In fact, it represents a repeated network consisting of WO_6 octahedra arranged across corners. The oxygen and W ions are placed in the center and corners of the octahedra, respectively, and each oxygen ion connects two octahedra (Fig. 2(a)).[47] Fig. 2(b) exhibits the corner- and edge-sharing modes as well as pentagonal columns mode. The ordered and coordinated structure may result in arrangement possibilities in the WO_3 lattice (Fig. 2(b)).[29] The band structure of a semiconductor can be altered due to the formation of oxygen deficiencies. The conduction band (CB) of WO_3 is formed by empty W 5d orbitals, while the valence band (VB) is formed by filled O 2p orbitals (Fig. 2(e)).[40] In $W_{18}O_{49}$, due to the formation of oxygen vacancies and subsequent ionization, new energy bands will be formed in its band gap, leading to higher conductivity relative to WO_3. Moreover, due to the formation of oxygen vacancies, the reduction of some W^{6+} ions occurs, resulting in the formation of shallow states below the CB due to formation of W^{5+}/W^{4+} energy levels (Fig. 2(e)). W^{5+}/W^{4+} would

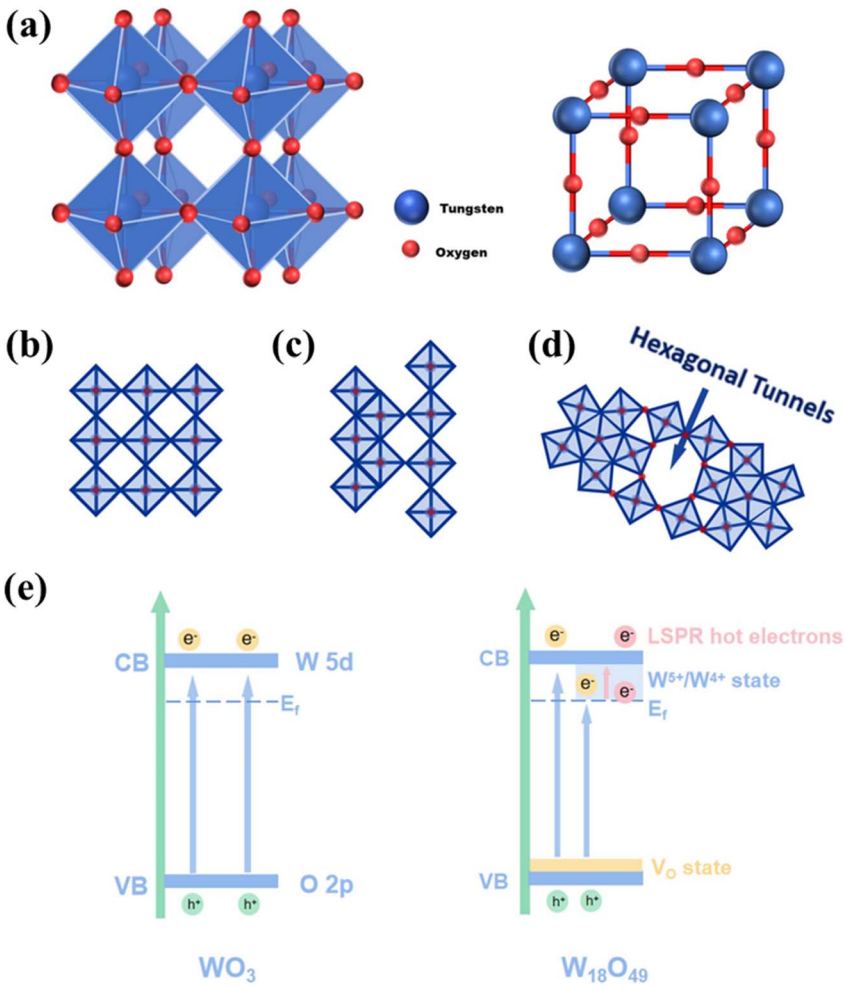

Fig. 2 (a) Structure of WO_3. (b) Corner- and (c) edge-sharing modes. (d) Pentagonal column mode. (e) Electronic band structure of WO_3 and $W_{18}O_{49}$.[44] Reproduced with permission from ref. 34. Copyright 2023, Elsevier.

capture the electrons excited by the oxygen vacancies, leading to polarization of the surrounding lattice and producing polarons.[31] The polarons will lead to the localized surface plasmon resonance (LSPR) effect. Owing to the special band structure of $W_{18}O_{49}$, it possesses photosensitive capability, and thus it can respond to almost the whole spectrum because of (i) the direct transition of electrons between its VB and CB; (ii) VB to W^{5+}/W^{4+} state transition, and (iii) LSPR effect. The special characteristics of $W_{18}O_{49}$ include the LSPR effect, photochromic effect, and narrow band gap. In particular, as stated before, the presence of oxygen vacancies leads to the generation of more free electrons, resulting in high electrical conductivity of $W_{18}O_{49}$, and thus it is a potential material for the fabrication of gas sensing devices.[14] The performance of $W_{18}O_{49}$-based gas sensors can be boosted by doping, decoration, formation of composites and morphological engineering. In the next sections, we discuss the gas sensing features of $W_{18}O_{49}$ gas sensors.

3. Pristine $W_{18}O_{49}$ gas sensors

In the solvothermal or hydrothermal methods, high temperature and pressure are used to accelerate the rate of reactions. Thus, they are highly promising synthesis methods for generating various nanostructures such as one-dimensional (1D) nanostructures. In this context, 1D $W_{18}O_{49}$ nanoneedles were produced *via* the solvothermal route at 160–220 °C for 3–9 h. Also, the solvent type (ethanol, propanol, butanol and cyclohexanol) and WCl_6 amount (60, 80, 100 and 120 mg) were changed to find the optimal conditions to achieve the highest response to NO_2 gas.[48] Regarding the solvent type, the highest sensing output was obtained when cyclohexanol was used due to the formation of uniform 1D nanoneedles with excellent crystallinity and substantial surface area of ~31 $m^2\ g^{-1}$, which were beneficial for surface redox reactions, hence enhancing the sensing performance. The response of $W_{18}O_{49}$ nanostructures was also affected by the WCl_6 dosage. Small WCl_6 dosages led to the accelerated the growth of $W_{18}O_{49}$ nanostructures along the (010) direction. Finally, this resulted in the generation of thin $W_{18}O_{49}$ nanoneedles, where the sample prepared using 100 mg WCl_6 possessed outstanding crystallinity and the best sensing properties. At a high WCl_6 dosage (120 mg), not only short/thick $W_{18}O_{49}$ nanostructures were formed but also their crystallinity decreased, which resulted in a decrease in their gas response. Furthermore, the solvothermal temperature affected the gas response. At 160 °C and 180 °C, thin $W_{18}O_{49}$ nanoneedles with agglomeration and poor crystallinity were synthesized. At 200 °C, almost perfect $W_{18}O_{49}$ nanoneedles with high crystallinity were formed, which exhibited an enhanced gas response. At 220 °C, $W_{18}O_{49}$ nanorods (NRs) or even block-shaped nanostructures were synthesized because of the accelerated growth rate at high temperature and the NO_2 response decreased. Regarding the solvothermal time, after 3 h reaction, long and thin $W_{18}O_{49}$ nanoneedles with poor crystallinity were synthesized. A longer solvothermal time to 5 h led to the formation of nanoneedles with high crystallinity, which eventually caused the highest response to NO_2 gas. A further increase in solvothermal time to 7 h resulted in the formation of short rod-like nanostructures with low crystallinity and low response to NO_2 gas. Overall, the sample solvothermally synthesized at 200 °C for 5 h showed that the use of cyclohexanol and WCl_6 dosage of 100 mg resulted in an enhanced gas response (R_g/R_a) of ~17 to 10 ppm NO_2 gas at 160 °C. Also, it exhibited excellent selectivity to NO_2 gas, which was related to the low bond dissociation energy of NO_2 gas (305 kJ mol^{-1}), which facilitated reactions with the absorbed

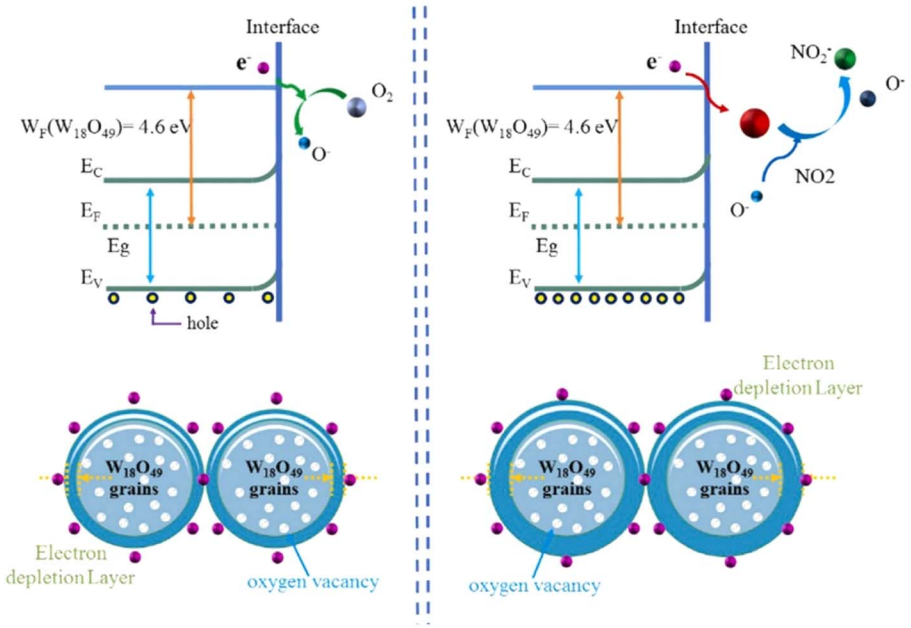

Fig. 3 Schematic of the NO_2 gas sensing mechanism of $W_{18}O_{49}$ nanoneedles.[48] Reproduced with permission from ref. 48. Copyright 2023, Elsevier.

oxygen ions. The improved response to NO_2 gas was related to following reasons: (i) due to the nonstoichiometric nature of $W_{18}O_{49}$, plenty of oxygen vacancies were generated in sensing materials, which acted as powerful adsorption sites for oxygen gas and (ii) due to the 1D nature of the $W_{18}O_{49}$ nanoneedles, not only a high surface area was created, but also the mobility of the charge carriers increased, while the recombination rate of charge carriers decreased. Fig. 3 schematically exhibits the sensing mechanism of the $W_{18}O_{49}$ sensor, in which initially an electron depletion layer (EDL) is formed in the presence of air by the adsorption of oxygen species and abstraction of electrons. Upon subsequent exposure to NO_2 gas, more electrons are extracted on the sensor surface, resulting in the expansion of the EDL and increase in the sensor resistance.

The detection of ammonia at low concentrations and RT is of high importance for clinical diagnosis and food safety.[49] In this regard, ultra-thin (less than 5 nm) $W_{18}O_{49}$ nanowires (NWs) with a high surface area of 151 $m^2\ g^{-1}$ were produced *via* the solvothermal method. Also, based on the photoluminescence (PL) study, a large amount of oxygen vacancies was formed during the hydrothermal synthesis of NWs. The sensor revealed a conductivity-type change with a change in the NH_3 amount. The n-to p-type behavior of the sensor was explained as follows: when the bulk donor density (N_D) was neither too high nor too low, then the surface state density (N_A) could reach the minimum with a variation in the gas concentration and a change in sign with a variation in conductivity was expected. Given that the diameter of the NWs was smaller than the Debye length of $W_{18}O_{49}$ at RT, when the bulk donor density of the NWs was in the appropriate range, an abnormal conductivity change was recorded. This sensor could detect sub ppm concentrations of NH_3 gas. The high response of the $W_{18}O_{49}$ NW sensor was due to the small diameter of the $W_{18}O_{49}$ NWs, creating a high surface area and non-stoichiometric nature due to the presence of a large amount of oxygen vacancies, which facilitated the chemisorption of oxygen at RT, resulting in a good response to NH_3 gas at RT.[50]

The reliable sensing of volatile organic compounds (VOCs) at RT is vital due to the toxic effect of some VOCs.[51] In this sense, 1D single crystalline $W_{18}O_{49}$ NRs with an aspect ratio of 20 were produced using a colloidal synthesis method for the detection of VOCs at RT.[52] The response ($[\Delta R/R_a] \times 100$) to 130 ppm ethanol was 3.5% at RT. However, the t_{rec} was too long, which was related to the RT sensing temperature. They used UV irradiation during the recovery period of the sensor and the t_{rec} significantly decreased. Also, the effect of the thickness of the sensing layer (1.2, 4.6, and 7.0 μm) was investigated and the 4.6 μm-thick sensor manifested the highest response. Also, the response time (t_{res}) and recovery time (t_{rec}) were not significantly different, which was related to the highly porous nature of $W_{18}O_{49}$ NRs.

Given that various crystal planes lead to various atomic surface structures and chemical and physical features, the sensing features of $W_{18}O_{49}$ with well-defined crystalline planes

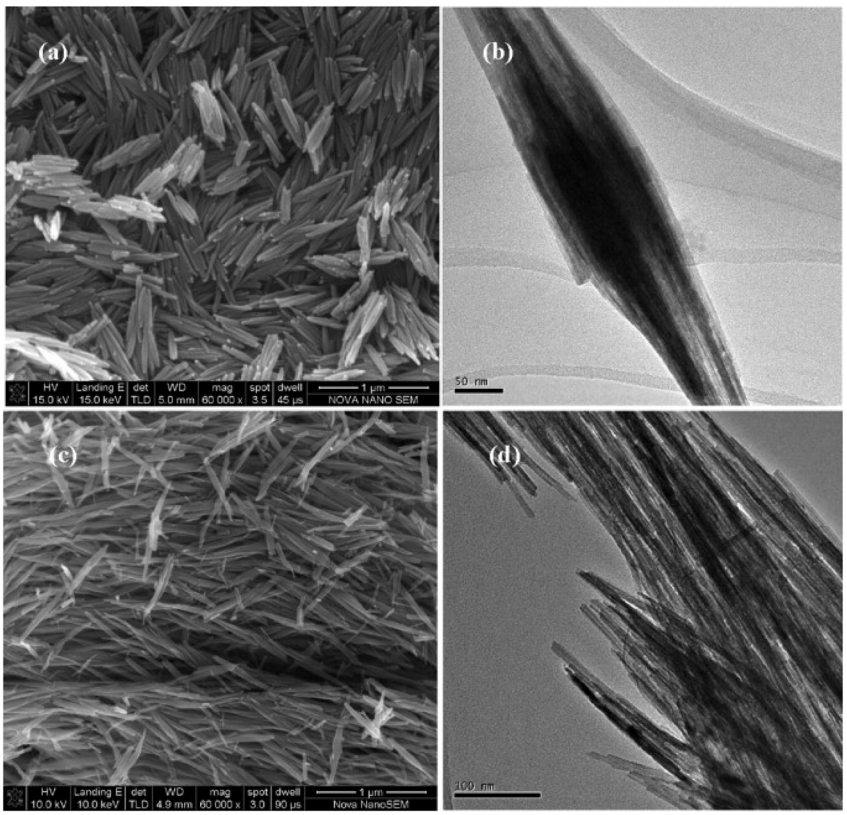

Fig. 4 SEM and TEM micrographs of the $W_{18}O_{49}$ (a) and (b) NRs and (c) and (d) NWs.[57] Reproduced with permission from ref. 57. Copyright 2011, Elsevier.

should be investigated. In this regards, Zhang *et al.*,[53] synthesized ultra-fine $W_{18}O_{49}$ NWs *via* a chemical synthesis approach, using WCl_6 and ethanol as the solvent. When the content of WCl_6 was 0.4 g, ultra-fine NW bundles with a large surface area of 194.7 m^2 g^{-1} and good crystallinity together with exposed (010) plane were formed. By increasing the content of WCl_6, sea urchin-like nanostructures were formed with a lower surface area and poor crystallinity. The response (R_a/R_g) of the ultra-fine NW bundle sensor to 50 ppm acetone was 48.6 at 280 °C, which was higher than that of other gas sensors, mainly owing to its high surface area and presence of abundant oxygen vacancies. According to DFT studies, the total adsorption energies for acetone gas are 80.60, 31.53 and 38.29 kJ mol^{-1} on the (010), (100) and (001) crystal planes, respectively. Thus, the (010) crystal plane had the greatest adsorption ability for acetone. Furthermore, acetone had the highest adsorption energy on the $W_{18}O_{49}$ (010) surface relative to other VOCs, which justified its good selectivity for acetone.

Mesocrystals can be formed by the oriented growth of pre-synthesized, well-defined building blocks, where the fusion of the building blocks results in the formation of crystalline structures with a porous nature,[54] which are highly promising for sensing studies. In an interesting study, $W_{18}O_{49}$ mesocrystals with a narrow size distribution (the diameter of ~250 nm and length of ~200 nm) were prepared by dissolving 200 mg WC_6 in 30 mL 1-butanol and subsequent solvothermal synthesis at 200 °C for 24 h. Alternatively, $W_{18}O_{49}$ NWs were prepared by dissolving the same amount WCl_6 in double the amount of 1-butanol, followed by the same solvothermal process.[55] The $W_{18}O_{49}$ mesocrystals had an average diameters of ~250 nm and average length of 200 nm. The mesocrystal sensor exhibited the maximum response (R_g/R_a) of 24.5 to 1 ppm NO_2, which was 5-times that of $W_{18}O_{49}$ NWs. The surface area of $W_{18}O_{49}$ mesocrystals was ~79 m^2 g^{-1}, while that of $W_{18}O_{49}$ NWs was 71 m^2 g^{-1}. Also, according to PL studies, more oxygen vacancies were present in the $W_{18}O_{49}$ mesocrystals than in the $W_{18}O_{49}$ NWs. Thus, although no significant difference between their surface areas was recorded, the higher amount of oxygen vacancies led to a noticeable difference in their sensing properties.

Given that in resistive gas sensors, gas molecules need to be absorbed on their surface, increasing the surface area of $W_{18}O_{49}$ is a good strategy to improve its properties as a sensor. Hence, it is expected that different morphologies of $W_{18}O_{49}$ will lead to different sensing properties due to their different surface areas.[56] In this regards, Qin *et al.*[57] solvothermally synthesized short and thick 1D NRs $W_{18}O_{49}$ using cyclohexane as the solvent at 200 °C/6 h. Also, long and thin $W_{18}O_{49}$ NWs were produced using 1-propanol as the solvent at 200 °C/9 h (Fig. 4).

The response (R_g/R_a) of $W_{18}O_{49}$ NWs and NRs were 140.7 and 131.5 to 5 ppm NO_2 at 150 °C, respectively. Also, $W_{18}O_{49}$ NWs exhibited faster dynamics relative to $W_{18}O_{49}$ NRs. The NWs had a larger surface area (~83.60 m^2 g^{-1}) than the NRs (~69.25 m^2 g^{-1}), which led to the availability of more adsorption sites on NWs for gases. Therefore, the NWs showed higher resistance modulation when exposed to NO_2 relative to $W_{18}O_{49}$ NRs.

Gu *et al.*[58] reported that isolated tungsten oxide NWs can be directly grown on a metallic W layer. In this context, aligned arrays of $W_{18}O_{49}$ NWs were directly synthesized *via* the *in situ* oxidation of a sputtered W layer on a substrate equipped with Pt electrodes (Fig. 5).[59] After the deposition of a tungsten film with a thickness of 150 nm, they were thermally oxidized at 550–750 °C under a continuous flow of argon and oxygen gases. At 550 °C, complete $W_{18}O_{49}$ NWs were not formed, while at 650 °C well-formed $W_{18}O_{49}$ NWs with small diameters (10 to 20 nm) were formed. Also at 750 °C, much thicker and longer NWs were formed.

Also, the effect of oxygen exposure time (0–60 min) during thermal oxidation at 650 °C was explored (Fig. 6(a)–(d)) and it was found that after exposure to oxygen for 60 min, the NWs possessed a length of 500 nm and diameter of 10–20 nm.

The sensor fabricated using $W_{18}O_{49}$ NW arrays at 650 °C for 60 min revealed a response (R_g/R_a) of 4.4 to 1 ppm NO_2 gas at 150 °C, with relatively fast t_{res} and t_{rec} of 78 and 32 s,

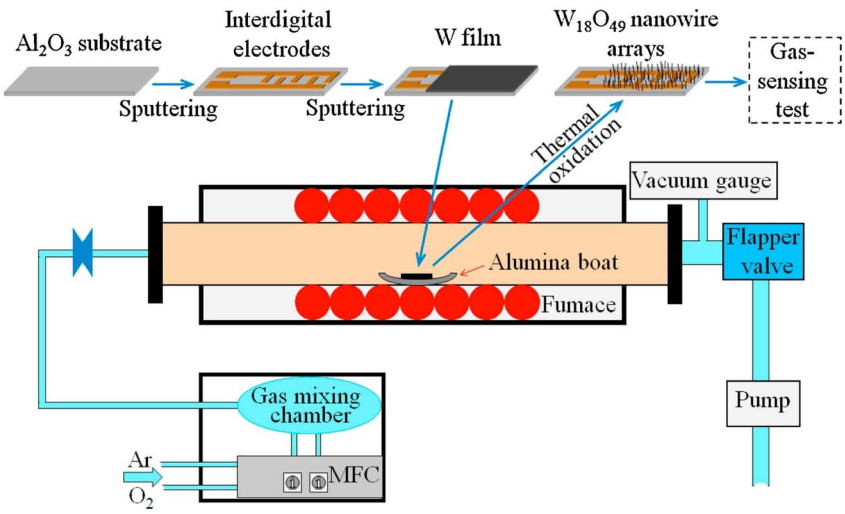

Fig. 5 Schematic of the synthesis of $W_{18}O_{49}$ NW arrays.[59] Reproduced with permission from ref. 59. Copyright 2016, Elsevier.

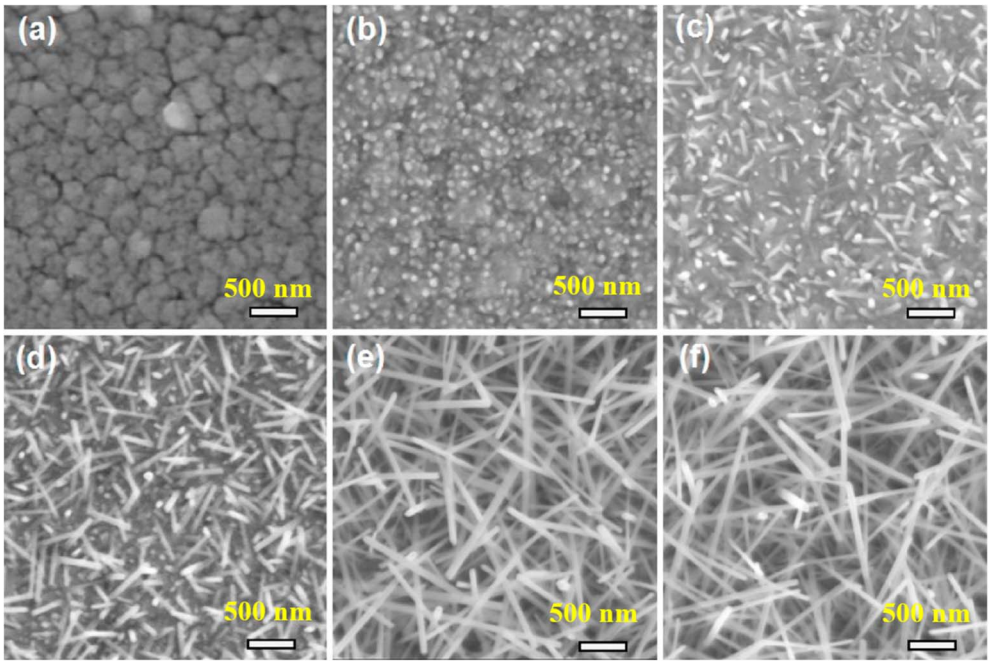

Fig. 6 SEM micrographs of $W_{18}O_{49}$ grown at 650 °C for various oxidation times under (a) no oxygen and oxygen flow time for (b) 10, (c) 20, (d) 40 and (e) 60 min and (f) in Ar/O_2 flow during growth.[59] Reproduced with permission from ref. 59. Copyright 2016, Elsevier.

respectively, which was attributed to the good diffusion of gas molecules in the NWs owing to their structural porosity. The rough alignment of the NWs resulted in formation of numerous NW/NW junctions, which served as electrical bridges between the electrodes. Also, in contact areas between NWs, potential barriers were formed in air, and upon subsequent exposure to NO_2 gas, great resistance modulation occurred.

As explained in this section, pristine $W_{18}O_{49}$ gas sensors are being used for detection of toxic gases; however, their performance can be further improved by noble metal decoration, which is explained in the next section.

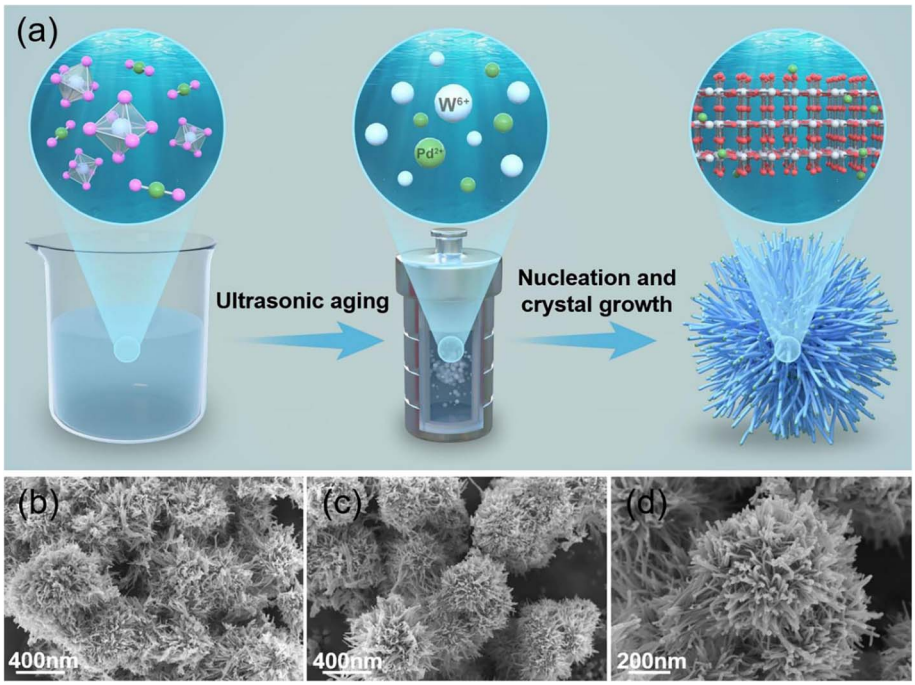

Fig. 7 (a) Synthesis procedure and SEM images of (a) $W_{18}O_{49}$ nanoflowers and (b–d) Pd (20 mg)-decorated $W_{18}O_{49}$ nanoflowers.[61] Reproduced with permission from ref. 61. Copyright 2023, Elsevier.

4. Noble metal decorated $W_{18}O_{49}$ gas sensors

Decoration of the sensing layer using noble metals is a good technique to boost the sensing performance, where the improved performance is related to the electronic and chemical sensitization impacts of noble metals.[60] In this regards, Pd-decorated flower-like $W_{18}O_{49}$ with an average diameter of 500 nm was prepared by Wang *et al.*[61] for the detection of formaldehyde (HCHO). Firstly, WCl_6 was added to an ethanol

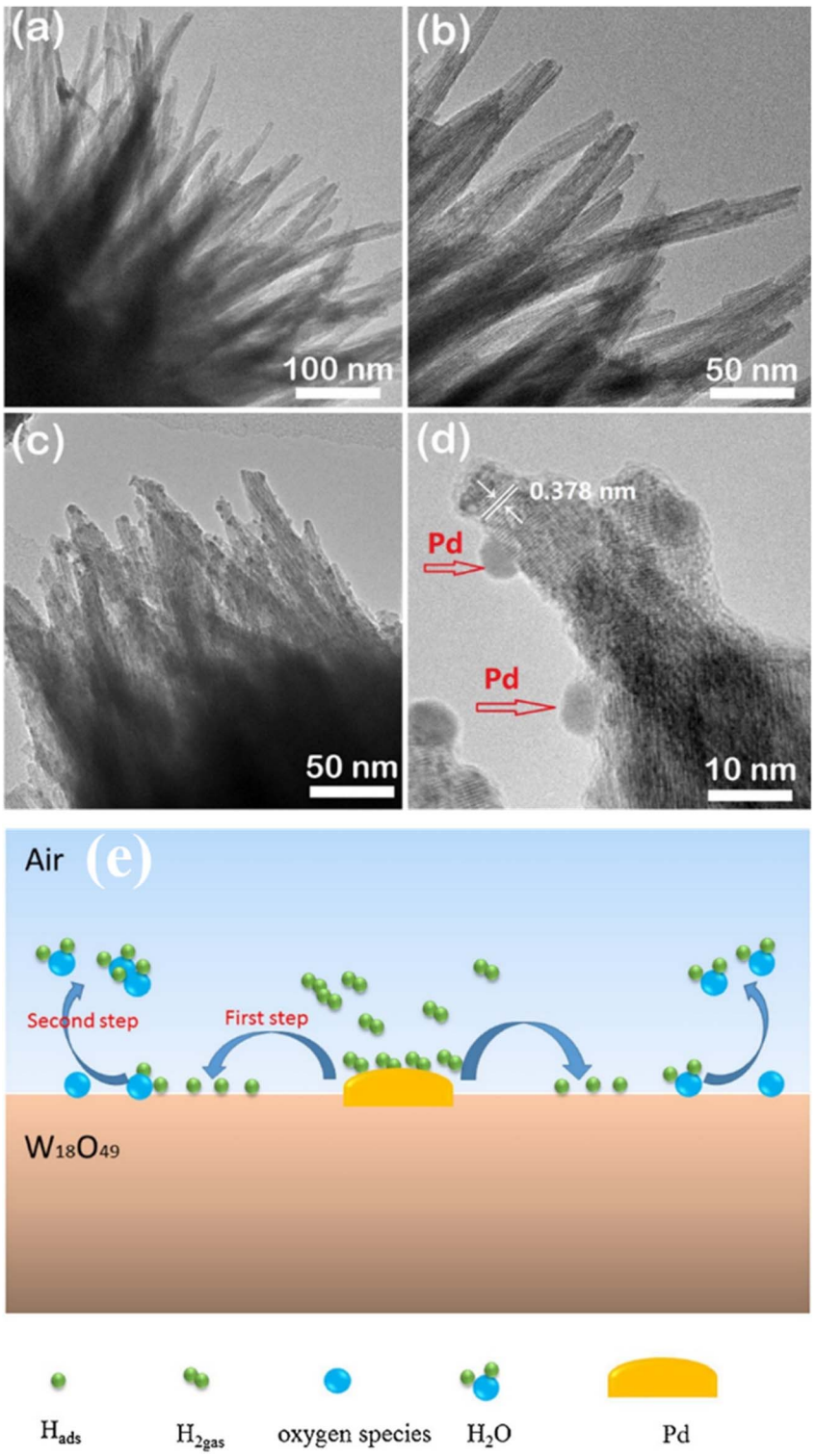

Fig. 8 TEM micrographs of (a) and (b) $W_{18}O_{49}$ and (c) Pd–$W_{18}O_{49}$. (d) HRTEM image of Pd–$W_{18}O_{49}$. (e) Schematic of the spillover effect.[63] Reproduced with permission from ref. 63. Copyright 2018, Elsevier.

solution and sonicated. Then, $PdCl_2$ (0, 20, 40, and 60 mg) was added, and after ultra-sonication for 0.5 h, the final products were synthesized by hydrothermal reaction at 180 °C/10 h (Fig. 7(a)). Both $W_{18}O_{49}$ and Pd (20 mg)-decorated $W_{18}O_{49}$ showed a flower-like morphology (Fig. 7(b)–(d)). The Pd (20 mg)-decorated $W_{18}O_{49}$ sensor displayed a high response (R_a/R_g) of 25.1 to 15 ppm formaldehyde at 180 °C, while the pristine sensor displayed a response of 12. The t_{res} was 16 s for the $W_{18}O_{49}$ sensor, while it was only 1 s for the Pd-decorated $W_{18}O_{49}$ sensor. Also, DFT calculations confirmed that the adsorption energy of formaldehyde on the Pd-sensitized $W_{18}O_{49}$ was −1.362 eV, which was stronger than that of $W_{18}O_{49}$ (−0.835 eV), implying that the adsorption of HCHO on the surface of $W_{18}O_{49}$ increased after Pd decoration. Furthermore, the superior sensor capacity of the Pd-decorated sensor was mainly related to the fact that this sensor had the highest amount of the oxygen vacancies, which acted as active sites for oxygen gas. In addition, the catalytic and electronic effects of Pd NPs, together with the flower-like morphology of $W_{18}O_{49}$ contributed to the sensing response.

Due to the highly explosive nature of H_2 gas, there is an urgent need to monitor the leakage of hydrogen to ensure human safety.[62] In this case, Pd is an excellent noble metal for H_2 sensing. It can not only easily dissociate H_2 gas molecules, but also adsorb up to 900-times its own volume of H_2 gas.[45] In this respect, urchin-like $W_{18}O_{49}$ was hydrothermally synthesized at 160 °C/24 h (Fig. 8(a) and (b)). Then, Pd NPs were decorated on urchin-like $W_{18}O_{49}$ using a chemical method, and subsequently the samples were annealed at 300 °C and 400 °C.[63] Based on the thermogravimetry analysis, at 400 °C, owing to the oxidation of $W_{18}O_{49}$ in the air, $W_{18}O_{49}$ was oxidized to WO_3 and Pd-decorated WO_3 was obtained. However, annealing at 300 °C resulted in the formation of Pd-decorated urchin-like $W_{18}O_{49}$ (Fig. 8(c) and (d)). The Pd-decorated $W_{18}O_{49}$ sensor had a high response (R_a/R_g) of 1600 to 0.1 vol% H_2 at 100 °C, while the Pd-decorated WO_3 sensor revealed a response of ~30. The boosted H_2 sensing performance was related to the 3D urchin-like hierarchical structure, which was beneficial for the easy and fast diffusion of H_2 gas in the in-depth parts of the sensor furthermore, $W_{18}O_{49}$ had many oxygen vacancies, which enhanced the adsorption of oxygen on the sensing layer. Finally, the spillover effect of Pd was responsible for the enhanced response. Firstly, in the presence of Pd NPs, H_2 molecules were dissociated into H species, and then they moved to $W_{18}O_{49}$, and finally reacted with the adsorbed oxygen ions on $W_{18}O_{49}$ (Fig. 8(e)),[64] as follows:

$$H_{2(ads)} \xrightarrow{Pd} 2H_{(ads)} \quad (1)$$

$$2H_{(ads)} + O_2^- \rightarrow H_2O + e^- \quad (2)$$

Networked $W_{18}O_{49}$ NWs with a diameter of ~50 nm and length of 2 μm were produced *via* the thermal evaporation of W powder at 1400–1450 °C for 10 min in the presence of oxygen.[65] Then, a Pt layer was sputtered on the $W_{18}O_{49}$ NW. The fabricated sensor was used in self-heating mode, and to minimize the power consumption, the samples were suspended with the bonding wires to reduce the dissipation of heat (Fig. 9(a)). Upon the application of a voltage, heat was generated inside the sensor due to the Joule heating effect (Fig. 9(b)). Accordingly, the response increased by applying a voltage due to the large amount of heat generated inside the sensor at high voltages. The selectivity of the sensor to H_2 gas was due to the dissociation of H_2 into H species by catalytic effect of Pt, and then their spill-over to the sensing layer.

Urchin-like $W_{18}O_{49}$ microstructures were synthesized *via* the hydrothermal route at 160 °C for 24 h. Later, Pt NPs were deposited on $W_{18}O_{49}$ *via* the UV illumination of an $H_2PtCl_6 \cdot 6H_2O$ solution. Under UV illumination, some W–O bonds were broken and the number of oxygen vacancies increased relative to the pristine $W_{18}O_{49}$. The surface area of $W_{18}O_{49}$ and Pt/$W_{18}O_{49}$ was ~48.90 and 53.70 $m^2\ g^{-1}$, respectively. Therefore, the surface area slightly increased after Pt decoration, which is beneficial for the sensing of gases. The pristine $W_{18}O_{49}$ displayed a response (R_a/R_g) of 7 to 10 ppm ethanol at 325 °C, while the Pt/$W_{18}O_{49}$ sensor displayed a response of 23 to the same amount of ethanol at 300 °C. Also, both sensors showed good selectivity to ethanol. According to DFT studies, the adsorption energies of ethanol on the $W_{18}O_{49}$ and Pt/$W_{18}O_{49}$ sensors (−0.85 and −1.18 eV) were higher than that for interfering gases, resulting in the better adsorption of ethanol relative to

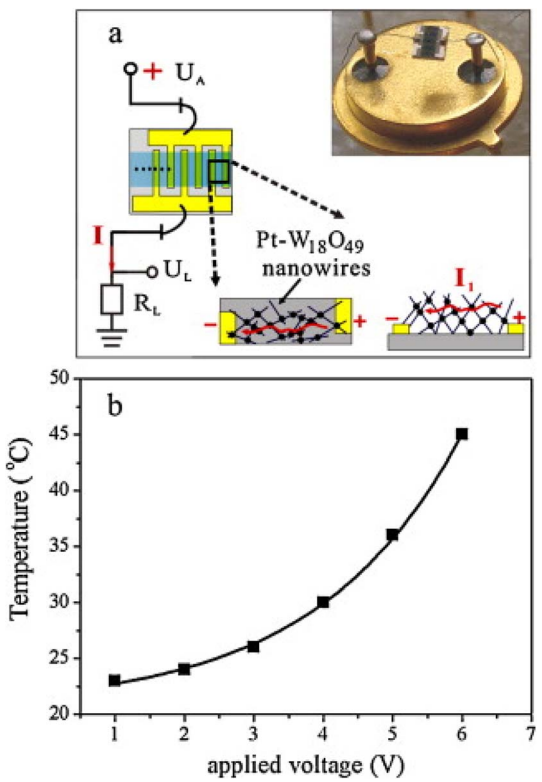

Fig. 9 (a) Schematic of the electrical set up for gas sensing measurement together with digital photo of the sensor. (b) Induced temperature of networked Pt–$W_{18}O_{49}$ NW *versus* the applied voltage.[65] Reproduced with permission from ref. 65. Copyright 2011, Elsevier.

interfering gases. Furthermore, the higher adsorption energy for ethanol on $W_{18}O_{49}$ indicated the superior adsorption ability of the Pd-decorated sensor for ethanol. Moreover, the adsorption energy for O_2 molecules on $W_{18}O_{49}$ and $Pt/W_{18}O_{49}$ was −2.31 and −3.41 eV, respectively, implying that $Pt/W_{18}O_{49}$ had higher adsorption ability for oxygen than $W_{18}O_{49}$. Due to the difference in work function between $W_{18}O_{49}$ and Pt, the Ohmic junctions were formed at the interface between $W_{18}O_{49}$ and Pt. Thus, in comparison with the $W_{18}O_{49}$ sensor, the flow of charge carriers in the Pt-decorated sensor was more favorable. To further study the behavior of the sensors, a fixed concentration of gas was extracted, and then injected into a gas chromatograph. It was revealed that the $Pt/W_{18}O_{49}$ sensor consumed more ethanol and generated more CO_2 relative to the $W_{18}O_{49}$ sensor. This was related to the catalytic effect of Pt towards the easy oxidation of ethanol.[66]

The major gases in a coal mines are CO, H_2S and CH_4.[67] Thus, it is important to realize gas sensors for the reliable sensing of these gases. In this context, Zhang *et al.*,[68] prepared $W_{18}O_{49}$ NWs using the solvothermal approach at 180 °C/24 h. Subsequently, Pd@Au core–shell bimetallic NPs (BNPs) were decorated on $W_{18}O_{49}$ NWs (Fig. 10) for sensing coal mine gases. The concentration of $HAuCl_4$ was set to 0.8, 1.3 and 1.8 mM, while that of Pd was fixed and the samples with the above-mentioned Au precursor concentrations were labelled as NWs/BNPs-1, NWs/BNPs-2, NWs/BNPs-3, respectively.

Owing to the interaction between Pd and $W_{18}O_{49}$ NWs, a small shift in the XPS spectrum was observed, which led to the regulation of the surface electronic characteristics of the $W_{18}O_{49}$ NW, and enhanced sensing features. The response (R_a/R_g) of the $W_{18}O_{49}$ NWs/BNP-2 sensor to H_2S (50 ppm) at 100 °C was about 55.5 with a weak response to CH_4 gas (Fig. 11(a)), while at 320 °C it had a response (R_a/R_g) of ~7.8 to 1000 ppm CH_4 (Fig. 11(b)). Thus, it was possible to tune the selectivity of the sensor to these gases by changing the temperature. In particular, CH_4 is a stable molecule because of its high molecule symmetry, accordingly its oxidation is difficult at low temperatures. With an increase in the working temperature, and due to the higher catalytic activity of BNPs, the oxidation of CH_4 molecules was accelerated. Furthermore, the sensor could successfully detect H_2S and CH_4 gases in mixed gases (50 ppm H_2S, NO, CO, and NH_3 as well as 1000 ppm CH_4) at their optimum temperature. The enhanced

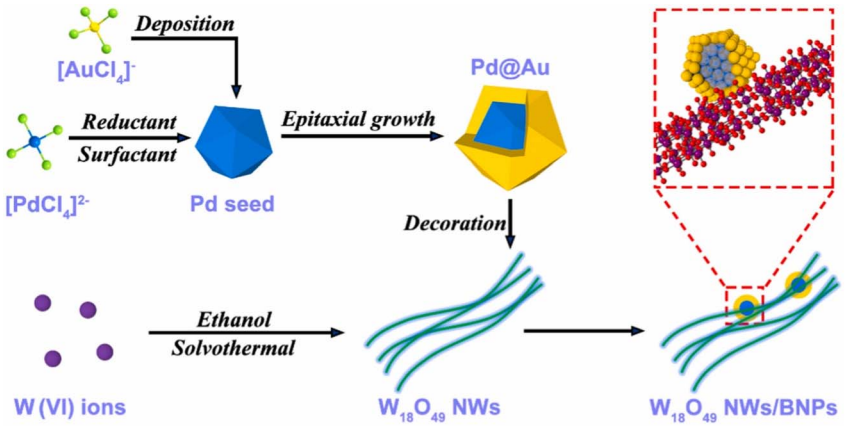

Fig. 10 Schematic representation of the synthesis of $W_{18}O_{49}$ NWs and $W_{18}O_{49}$ NWs/BNPs.[68] Reproduced with permission from ref. 68. Copyright 2022, Elsevier.

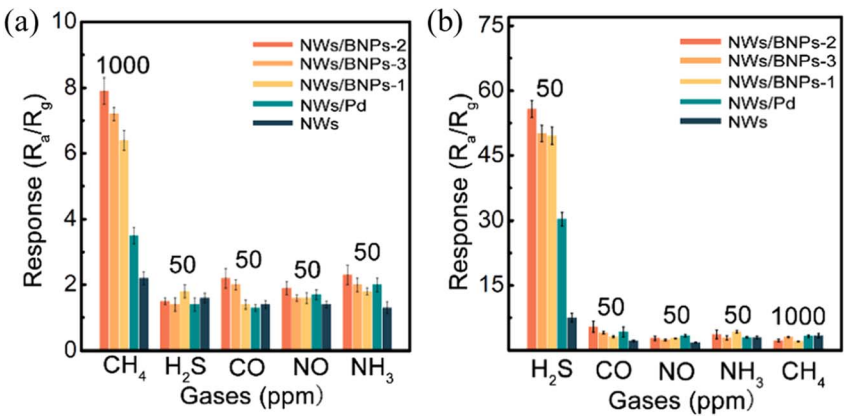

Fig. 11 Selectivity of $W_{18}O_{49}$ NWs/BNPs-2 at (a) 320 °C and (b) 100 °C to various gases.[68] Reproduced with permission from ref. 68. Copyright 2022, Elsevier.

features of the sensor were related to (i) the ultra-fine 1D NWs with diameters less than 1 nm, which provided more adsorption sites and fast transport channels, and the presence of a large amount of oxygen vacancies, (ii) catalytic effects of Au and Pd NPs towards the target gases and (iii) formation of potential barriers between the bimetallic NPs and sensing materials and modulation of the potential barriers in an atmosphere containing target gases.

Hollow nanostructures offer a higher surface area relative to bulk materials due to the availability of both inner and outer walls for gas adsorption. Therefore, they should possess a high response to target gases. Xu *et al.*[69] constructed hollow $W_{18}O_{49}$ spheres *via* the hydrothermal route at 180 °C/16 h. Subsequently, Co_3O_4/hollow $W_{18}O_{49}$ spheres were prepared *via* the chemical route by adding a Co precursor to hollow $W_{18}O_{49}$ spheres. Finally, Au was decorated on Co_3O_4/hollow $W_{18}O_{49}$ spheres using a chemical method. The hollow structure consisted of lamellar flakes, which formed porous and large spheres (Fig. 12).

The response (R_a/R_g) of the Au-decorated $Co_3O_4/W_{18}O_{49}$ sensor to 2 ppm TEA at 270 °C was to 16.7, which was significantly higher than that of $Co_3O_4/W_{18}O_{49}$ (11.3) and $W_{18}O_{49}$ (3.9). Firstly, the porous and hollow structure provided a high surface area (76.12 $m^2\ g^{-1}$), which led to the availability of more active sites for the adsorption of oxygen molecules. Besides, the porous and hollow nature contributed to fast gas diffusion (Fig. 13(a)). Secondly, the Au NPs were a highly active catalyst for oxygen dissociation due to the spillover effect (Fig. 13(b)). Therefore, TEA easily reacted with the adsorbed oxygen ions and electrons were released to the sensor surface (Fig. 13(c)). Thirdly, the formation of p–n heterojunctions at the interface between p-type Co_3O_4 and n-type $W_{18}O_{49}$ contributed to the enhancement in the sensing performance. The work function of Co_3O_4 and $W_{18}O_{49}$ was 6.1, and 4.6 eV, respectively.[70–72] Hence, their Fermi levels were equal due to the flow of electrons from $W_{18}O_{49}$ to Co_3O_4. This resulted in the widening of the EDL, and at the interface of heterojunctions, potential barriers were created with band bending. Therefore, owing to the large baseline resistance, a remarkable reduction in resistance occurred upon exposure to TEA gas.

Sun *et al.*,[73] initially prepared $W_{18}O_{49}$ NRs *via* a solvothermal reaction at 200 °C for 8 h, and then Ag/AgCl NPs were decorated on the $W_{18}O_{49}$ NRs using $AgNO_3$ as the precursor and irradiation with an Xe lamp. The response (R_a/R_g) of the sensor was 115.5 to 100 ppm H_2S at 300 °C and t_{res} and t_{rec} were 21 and 26 s, respectively. The improved gas-sensing capacity relative to the pristine sensor was attributed to catalytic effect of Ag NPs owing to the spillover effect,[74] as well as the electronic effect due to the formation of potential barriers in the contact areas between Ag/AgCl and $W_{18}O_{49}$.

Alloy nanocrystals not only have the unique characteristics of each metal, but also additional features due to the synergy between different atoms. In particular, they provide boosted catalytic properties for gases, which can significantly enhance

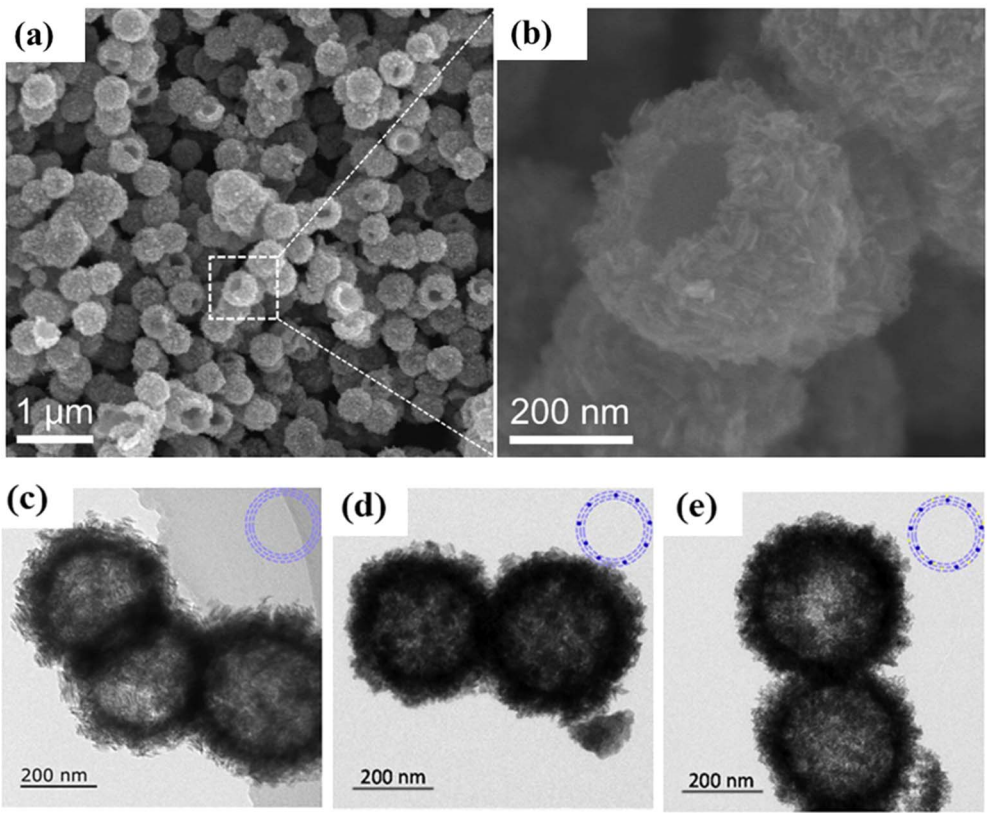

Fig. 12 (a) and (b) SEM micrographs of $W_{18}O_{49}$ hollow spheres. TEM images of (c) $W_{18}O_{49}$, (d) $Co_3O_4/W_{18}O_{49}$, and (e) Au-decorated $Co_3O_4/W_{18}O_{49}$ hollow spheres.[69] Reproduced with permission from ref. 69. Copyright 2019, Elsevier.

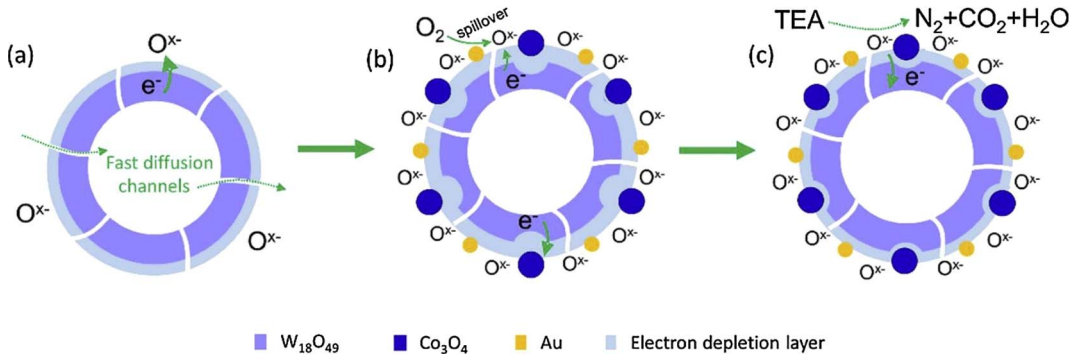

Fig. 13 Schematic of (a) pristine $W_{18}O_{49}$ in air, (b) and (c) Au-decorated $Co_3O_4/W_{18}O_{49}$ in air and TEA gas.[70] Reproduced with permission from ref. 70. Copyright 2019, Elsevier.

the catalytic performance of the sensor. In the study conducted by Bai *et al.*,[75] initially urchin-like $W_{18}O_{49}$ was hydrothermally prepared at 180 °C/24 h. Then, the $Au_{39}Rh_{61}$ alloy was synthesized *via* the co-precipitation method, and finally $Au_{39}Rh_{61}$ alloy-decorated $W_{18}O_{49}$ was prepared using a chemical method for *n*-butanol sensing. At 260 °C, the response (R_a/R_g) of the $Au_{39}Rh_{61}$–$W_{18}O_{49}$ sensor was ~11 to 50 ppm *n*-butanol, which was 4-fold higher than that of Au–$W_{18}O_{49}$ (~2.2) and 2-times higher than Rh–$W_{18}O_{49}$ (~5.1) sensor. The increased gas sensing properties of the Au_xRh_{1-x}-decorated $W_{18}O_{49}$ was related to (i) its large surface area due to its urchin-like morphology, (ii) spillover effect of $Au_{39}Rh_{61}$ alloy, where the dissociation of molecular oxygen due to the catalytic effect of the noble metals resulted in activated oxygen species, which were spilt over on the sensing layer and (iii) formation of Schottky barriers between the noble metals and sensing layer.[76]

5. Doped $W_{18}O_{49}$ gas sensors

Doping with metal atoms is an efficient approach to modify the electronic characteristics of materials *via* the introduction of additional energy levels, creation of oxygen vacancies and increasing the surface adsorption/desorption capability.[77,78] Doping of $W_{18}O_{49}$ with metals such as Mo, Fe, Pd and Ni led to the generation of oxygen vacancies, which eventually led to an enhanced gas response.[63,79–82]

Acetone is a biomarker gas and the amount of acetone in exhaled breath can be used for the diagnosis of diabetic patients, where its content in healthy people is ~0.3–0.9 ppm and increases to 1.8 ppm in diabetic patients. In this regards, $Pd_xW_{18}O_{49}$ (x = 1.83%, 3.60%, 7.18%, and 11.69%) NWs, were synthesized *via* the hydrothermal method. All the Pd-doped samples showed an NW morphology without a significant difference in surface morphology. Also, based on the XPS study, the $Pd_{7.18\%}W_{18}O_{49}$ NWs had the largest oxygen vacancy content among the samples. Also, this sample displayed the highest response (R_a/R_g) of ~146 to 50 ppm acetone at 175 °C, with the fast t_{res} and t_{rec} of 5 and 10 s, respectively.[81] The short dynamics of the optimized gas sensor was related to its relatively high sensing temperature, which provided more energy to facilitate the flow of electrons. Also, this sensor exhibited a reliable response to acetone in a mixed gas comprised of ethanol and acetone, which is important for medical diagnosis applications. The improved gas sensing was related to the formation of Schottky barriers between Pd and $W_{18}O_{49}$ NWs and existence of the highest amount of oxygen vacancies, which favored the adsorption of oxygen on the sensor surface. Accordingly, the reactions between acetone and adsorbed oxygen ions lead to the generation of a higher sensing signal.

In an interesting study, rambutan-like Ni-doped $W_{18}O_{49}$ was fabricated *via* a one-step solvothermal route. The specific surface area of $W_{18}O_{49}$ and $Ni_{0.05}W_{18}O_{49}$ was ~76 $m^2\ g^{-1}$ and 130.5 $m^2\ g^{-1}$, respectively. The $Ni_xW_{18}O_{49}$ sensor with $x = 0.05$ Ni-doping displayed a response (R_g/R_a) of 182 to 50 ppm *n*-butanol at 160 °C with a short t_{res} and t_{rec} (14 s/241 s), respectively, while the response of the pristine sensor was 26.7. The improved response of the doped sensor was correlated with the increase in the amount of oxygen vacancies due to Ni-doping and high surface area (130.5 $m^2\ g^{-1}$).[83]

Simultaneously doping two metals in tungsten oxides has rarely been reported. The introduction of two dopants with different sizes and valences into host materials can change their electronic features, create more oxygen vacancies, and improve their catalytic activity.[84] In this context, the impact of Co and Ni co-doping in $W_{18}O_{49}$ was investigated for the detection of TEA.[85] Co and Ni-doped porous $W_{18}O_{49}$ nano-urchins with a surface area of ~165.85 $m^2\ g^{-1}$ were achieved using the solvothermal method at 180 °C/24 h. At 250 °C, the sensor with 1 wt% Co and 2 wt% Ni $W_{18}O_{49}$ displayed a response (R_a/R_g) of 114 to 50 ppm TEA, which was higher than that of the single-doped and undoped $W_{18}O_{49}$ sensors. The enhanced response was related to the hierarchical urchin-like structure of the sensor, its high surface area and effects of the co-doped metal ions.[86] As p-type dopants, Co and Ni replaced W in the $W_{18}O_{49}$ lattice and created oxygen vacancies. Thus, more O_2 molecules were adsorbed on the surface, and therefore more reactions with TEA occurred. Besides, the oxidization of Co and Ni dopants reversibly transferred electrons at the interface of $W_{18}O_{49}$ with NiO or Co_2O_3 as (Ni ⇆ NiO and/or Co ⇆ Co_2O_3), forming a p–n heterojunction, resulting in high electrical resistance, and upon exposure to TEA, the release of electrons resulted in a remarkable change in resistance. Furthermore, dopants lowered the band gap and

promoted the charge flow kinetics, and hence increased the reactivity to TEA molecules. Also, the C–N bond in TEA had the lowest bonding energy and easily broke and participated in redox reactions at the sensing temperature. Extra doping of Co and Ni (>3 wt%) resulted in intensive contraction/deformation in the $W_{18}O_{49}$ lattice and reduced the electrical conductivity or even caused the segregation of the dopant cations and formation of NiO and Co_3O_4. Accordingly, the sensing performance decreased when high amounts of dopant were used.

Prior studies revealed that the d-band center of materials is related to their adsorption activity, where a higher energy level of the d-band center results in enhanced activity.[87] Based on DFT results, the density of state (DOS) indicated that the doping of Ni and Co led to a shift in DOS from a low to high energy level, indicating an upward shifting of the d-band center (Fig. 14(a) and (b)). Thus, the adsorption ability of the sensor increased after co-doping. Also, based on the DFT analysis, the adsorption energy of TEA on Ni and Co co-doped $W_{18}O_{49}$ ($E_{ad} = -1.53$ eV) was much higher than the pristine $W_{18}O_{49}$ ($E_{ad} = -0.79$ eV) (Fig. 14(c) and (d)), which was consistent with the experimental results.

Ti was added to $W_{18}O_{49}$ after and during the growth of $W_{18}O_{49}$ NWs. Before the hydrothermal growth of the $W_{18}O_{49}$ NWs, Ti (2 at%) was added as $TiCl_4$ to the final solution. Also, after the hydrothermal growth of the $W_{18}O_{49}$ NWs, using physical impregnation, Ti (0.6, 2, and 6 at%) was added to NWs using $TiCl_4$.[88] The pristine $W_{18}O_{49}$ NWs had an average diameter of ~80 nm and average length of 900 nm (Fig. 15(a)). The Ti-added $W_{18}O_{49}$ NWs prepared *via* the physical impregnation method retained the morphology of the pristine $W_{18}O_{49}$ NWs, whereas the addition of Ti during solvothermal growth inhibited the growth of the $W_{18}O_{49}$ NWs, and finally $W_{18}O_{49}$ bundles were formed (Fig. 15(b)). Both Ti-added $W_{18}O_{49}$ sensors showed a p- to n-type transition with an increase in the temperature to 90 °C (Fig. 15(c)). The abnormal p-type feature observed at low temperature was due to the generation of an inversion layer at the surface of the n-type $W_{18}O_{49}$ NWs, originating from the intensive surface adsorption of oxygen due to the high density of surface states. In fact, the surface of nonstoichiometric $W_{18}O_{49}$ NWs was very active owing to the existence of a large amount of oxygen vacancies. When the additive was added to the $W_{18}O_{49}$ NWs a new energy level was created inside the band gap. Thus, the gas adsorption improved because of the presence of additional surface states. The intensive adsorption of oxygen on the NW surface caused a change in the Fermi level energy of the $W_{18}O_{49}$ NWs, resulting in the appearance of an inversion layer. Among the sensors, the sensor with 2% Ti prepared *via* physical impregnation displayed the highest response to NO_2 gas at RT (Fig. 15(d)) because the physical impregnation method led to the formation of a random dispersion of small TiO_2 particles, which increased the adsorption activity for oxygen on the surface of the sensing material. Also, the Ti-doped sample prepared *via* chemical synthesis revealed a lower response due to the fact that the $W_{18}O_{49}$ bundles inhibited the fast diffusion of NO_2 to the in-depth parts of the bundles.

6. Composite-based $W_{18}O_{49}$ gas sensors

In composite gas sensors, numerous heterojunctions between different materials can be formed, which cause a remarkable modulation in their electrical resistance.[13] 2D graphene, which

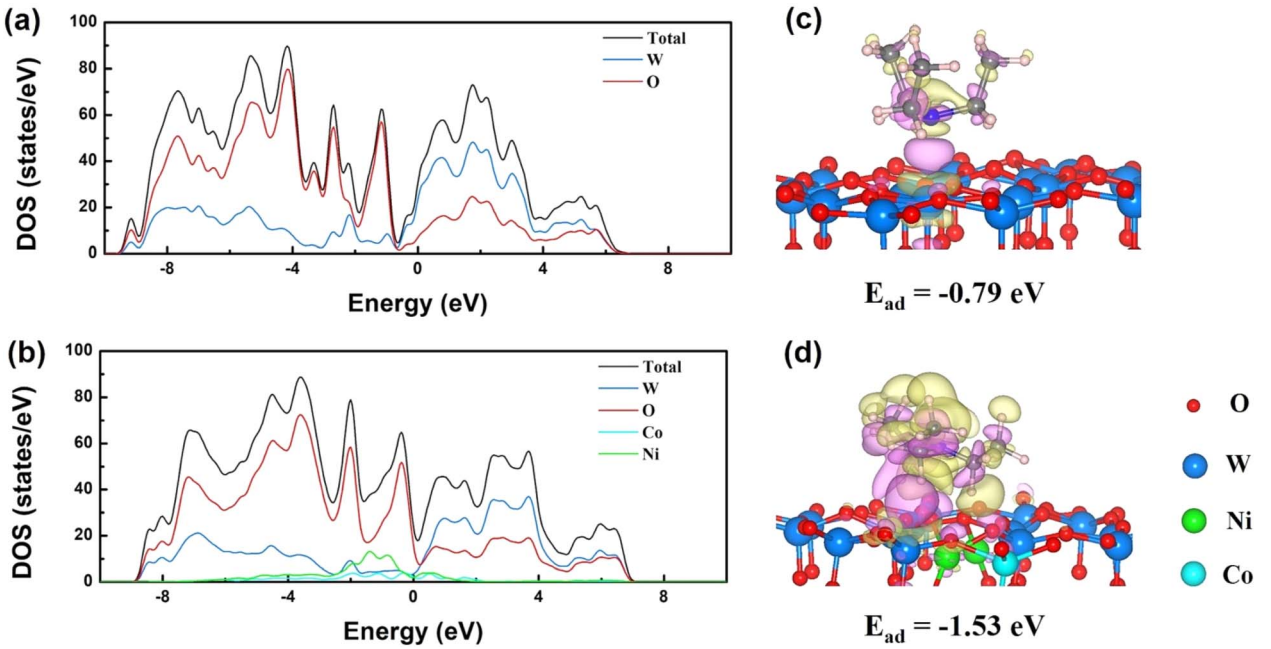

Fig. 14 DOS of (a) the $W_{18}O_{49}$ and (b) Co and Ni co-doped $W_{18}O_{49}$ (010) surfaces. Charge density difference of the adsorption configuration of TEA on (c) $W_{18}O_{49}$ and (d) Co and Ni co-doped $W_{18}O_{49}$ (010) surface.[85] Reproduced with permission from ref. 85. Copyright 2023, Elsevier.

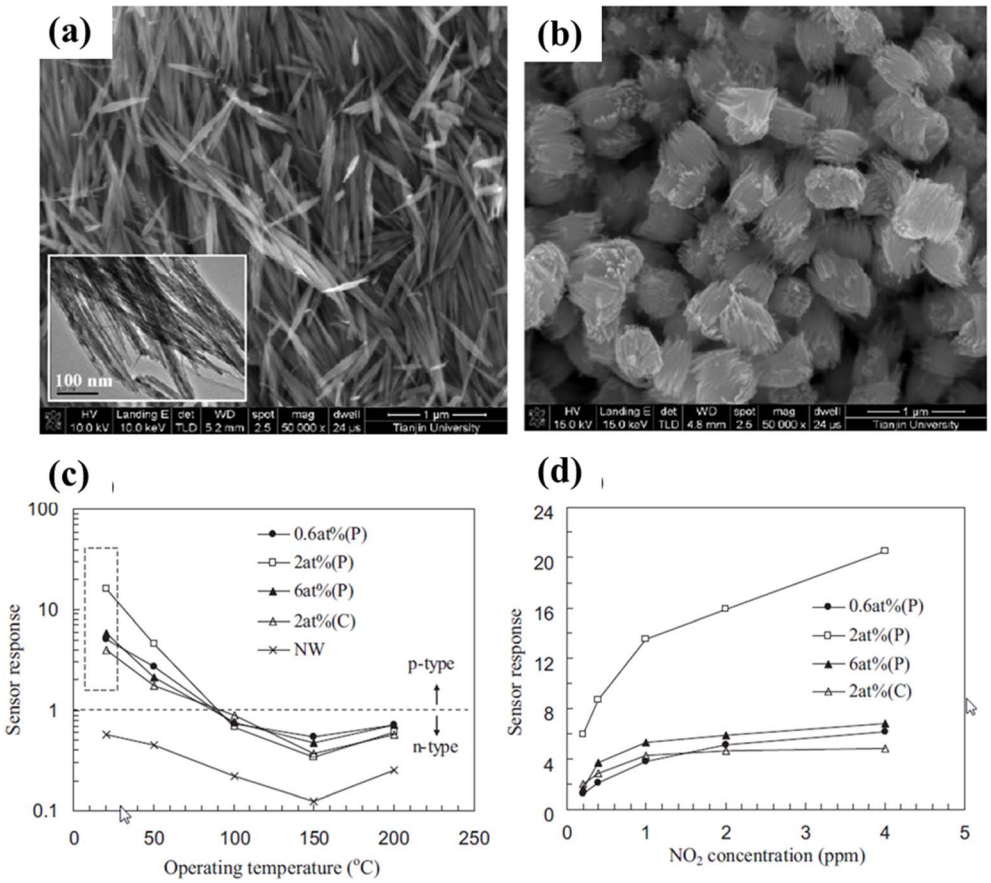

Fig. 15 SEM images of (a) pristine $W_{18}O_{49}$ NWs and (b) Ti-added $W_{18}O_{49}$ NWs prepared using a chemical synthesis method. (c) Sensor responses *vs.* temperature for pristine and Ti-added $W_{18}O_{49}$ NWs to 2 ppm NO_2 and (d) corresponding calibration curves.[88] P stands for physical impregnation and C stands for chemical addition of Ti. Reproduced with permission from ref. 88. Copyright 2012, Elsevier.

consists of C atoms with sp^2 hybridization, together with abundant defects and functional groups, high carrier mobility and high electrical conductivity,[89] is a promising material for sensing studies. Qiu *et al.*[90] prepared $W_{18}O_{49}$/graphene nanocomposites (with the graphene concentration of 0.005, 0.01, and 0.015 mg L^{-1}) using the hydrothermal technique at 180 °C/24 h. The composites were comprised of interlaced NWs with diameters of 30–60 nm and lengths of 1–2 μm. The response (R_a/R_g) of the $W_{18}O_{49}$/graphene (0.01 mg L^{-1}) sensor was 16.47 to 100 ppm ethanol at 340 °C, with t_{res} and t_{rec} of 1 and 11 s, respectively. A higher amount of graphene in the composite resulted in high conductivity, which eventually suppressed the variation in resistance in the fabricated sensor. The high sensing performance of the optimal sensor was related to its high active surface area (~42.35 m^2 g^{-1}), which provided abundant active sites for ethanol molecules. Also, due to the n- and p-type nature of $W_{18}O_{49}$ and graphene, p–n heterojunctions were formed at the interfaces between the two semiconductors, resulting in the significant modulation of the resistance. Furthermore, double Schottky barriers were created in the contact areas between the $W_{18}O_{49}$ grains, where the flow of electrons was difficult between the grains in air (Fig. 16(a)). In an ethanol atmosphere and due to the release of electrons, the height of the double Schottky barriers decreased and caused a remarkable change in resistance (Fig. 16(b)). Also, because of the difference between the work functions of graphene and $W_{18}O_{49}$, localized p–n heterojunctions were created at the interface of the composite materials, with formation of potential barriers in air, which are considered powerful sources of resistance modulation,[91,92] remarkably modulating the resistance in an ethanol atmosphere. Furthermore, some structural defects were produced in the interface areas between the two materials, which acted as potential sites for the adsorption of ethanol.

Transition metal dichalcogenides (TMDs) with the general formula of MX_2 (M = transition metal; X= S, Se, and Te) have a small band gap, good conductivity, and edge-exposed sites, leading to good binding interactions with gas molecules.[93] In this respect, a $WS_2/W_{18}O_{49}$ heterojunction was synthesized *via* the pyrolysis of WO_3 in the presence of sulfur (S) powder, thiourea (CH_4N_2S), and a mixture of "S" and CH_4N_2S at 850 °C for 1–4 h in an Ar atmosphere. The pyrolysis of WO_3 using a mixture of "S" and CH_4N_2S yielded WS_2 and $W_{18}O_{49}$ heterojunctions and exhibited superior gas-sensing properties. After 1 h of pyrolysis, agglomerated WS_2 covered the $W_{18}O_{49}$ nanorods. By performing pyrolysis for 2 h, the amount of NRs

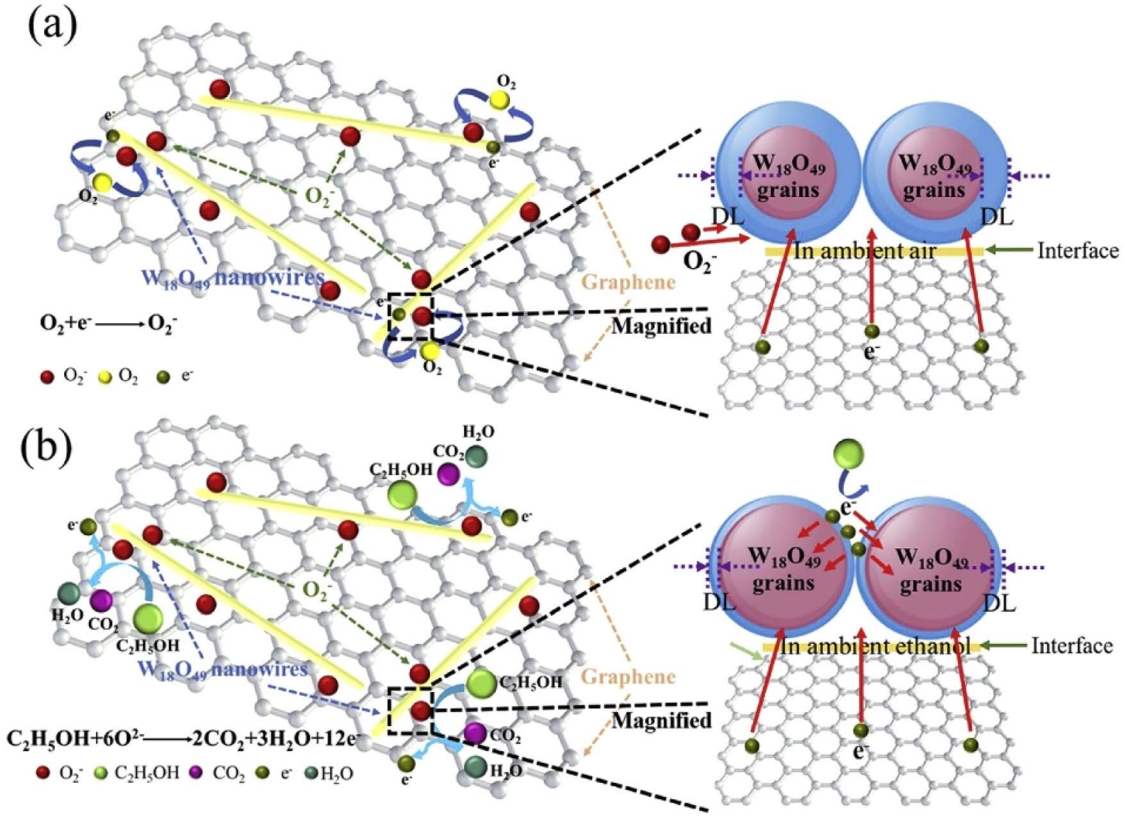

Fig. 16 (a) Schematic of the sensing mechanism of $W_{18}O_{49}$/graphene in air (b) and (c) ethanol.[90] Reproduced with permission from ref. 90. Copyright 2021, Elsevier.

increased because of the diffusion of "S" vapor into the core parts of WO_3. After pyrolysis for 3 and 4 h, the formation of $W_{18}O_{49}$ NRs increased, with less agglomeration of WS_2. The sensor fabricated from the sample after 3 h pyrolysis exhibited an enhanced response [$(\Delta R/R_a) \times 100$] of 25.7% and 35.67% to 5 ppm NH_3 and NO_x gases, respectively, at RT. The sensor displayed p-type behavior because of the p-type nature of WS_2. The edge-exposed W atoms in WS_2 were highly reactive to gases due to the high electron density of the d-orbitals in W atoms. Furthermore, the formation of p–n heterojunctions between $W_{18}O_{49}$ and WO_3 resulted in the modulation of the electrical resistance of the sensor in the presence of gases.[94]

MXenes are 2D transition metal carbides/nitrides with the formula of $M_{n+1}X_nT_x$, where M is a transition metal, X is a carbon or N atom and T_x stands for surface functional groups. Due to their high conductivity, high surface area and presence of functional groups, they are very promising sensing materials.[95] In this case, $W_{18}O_{49}/Ti_3C_2T_x$ MXene nanocomposites with 1, 1.5,2 and 2.5 wt% MXene were fabricated *via* the *in situ* growth of 1D $W_{18}O_{49}$ NRs on the surface of 2D $Ti_3C_2T_x$ MXene NSs through the solvothermal route at 150 °C/24 h.[96] The $W_{18}O_{49}/Ti_3C_2T_x$ composite containing 2 wt% $Ti_3C_2T_x$ displayed a response (R_g/R_a) of 11.6 to 20 ppm acetone gas at 300 °C with fast t_{res} and t_{rec} of ~10.5 and ~26 s, respectively. Furthermore, it could detect 170 ppb acetone, which was lower than the concentration of acetone in the exhaled breath of diabetic people.[97] The enhanced gas sensing performance was related to the presence of MXene with a high amount of surface groups such as –O and –OH, which are considered potential sites for the adsorption of acetone molecules. Also, Schottky junctions were formed between MXene and $W_{18}O_{49}$, and therefore the sensor experienced a larger resistance variation than that of the $W_{18}O_{49}$ sensor when it was exposed to acetone. The decrease in response with a higher content of MXene was due to the presence of –F groups on the MXene surface, which had negative effects on the gas sensing. Furthermore, a high amount of MXene resulted in stacking of the MXene NSs, which decreased the surface area for the adsorption of gas molecules.

Conducting polymers (CPs) have high conductivity, good flexibility, tunable properties and can be used for the detection of gases at RT.[98] In this regards, polypyrrole (PPy)@$W_{18}O_{49}$ C–S NRs were fabricated *via* the *in situ* polymerization of pyrrole monomer on solvothermally synthesized $W_{18}O_{49}$ NRs.[99] The thickness of PPy was 5, 10 and 18 nm over $W_{18}O_{49}$ NRs with a diameter of ~60 nm. The response (R_a/R_g) of the fabricated sensor (Fig. 17(a)) with a PPy shell thickness of 5 nm was 4.1 to 20 ppm NH_3 at 15 °C. Furthermore, it could also detect 1 ppm NH_3, which is below the human toxicity level, *i.e.* 25 ppm.[100] Three types of junctions were present in the sensor, *i.e.*, homojunctions between PPy in the contact areas between C–S NRs, PPy shell boundary and PPy-$W_{18}O_{49}$ heterojunctions (Fig. 17(b)). Owing to the modulation of the potential barriers in

these junctions in the presence of NH_3, and particularly heterojunctions (Fig. 17(c) and (d)), a high response was observed. In fact, when NH_3 was adsorbed on the PPy shell, proton transfer and electron transfer occurred between the PPy and NH_3 molecules, leading to a decrease of the hole concentration in the p-type PPy shell, which resulted in an increase in the height of the potential barriers and increase in the resistance of the PPy shell. The larger response of the sensor with a thinner shell was related to the complete depletion of the shell layer from charge carriers, and upon subsequent exposure to NH_3, significant modulation of the resistance occurred (Fig. 17(e)).

The fabrication of 1D C–S arrays with a uniform shell layer and high alignment over their entire surface is attractive for realizing gas sensors with an excellent performance. In the study by Qin *et al.*,[101] a W layer with a thickness of ~100 nm was first sputtered on a substrate. Then, roughly aligned $W_{18}O_{49}$ NWs (15 to 20 nm) were selectively grown on the substrate *via* thermal oxidation at 650 °C for 1 h. The intercrossing of NWs formed numerous NW–NW junctions, which acted as potential barriers and were considered powerful sources of resistance modulation. Then, a Ti film with thicknesses of 3 and 6 nm was sputter-deposited on $W_{18}O_{49}$. Upon annealing at 450 °C for 1 h, crystalline $W_{18}O_{49}$–TiO_2 C–S NWs were synthesized. The sensor with a TiO_2 shell thickness of 6 nm revealed a higher response (R_g/R_a) of 36.5 to 5 ppm NO_2 gas at RT. Interestingly, both C–S sensors exhibited a p-type feature at RT, despite the n-type semiconductor behavior of both the $W_{18}O_{49}$ and TiO_2 materials, which was observed in other metal oxides.[102,103] In fact, the

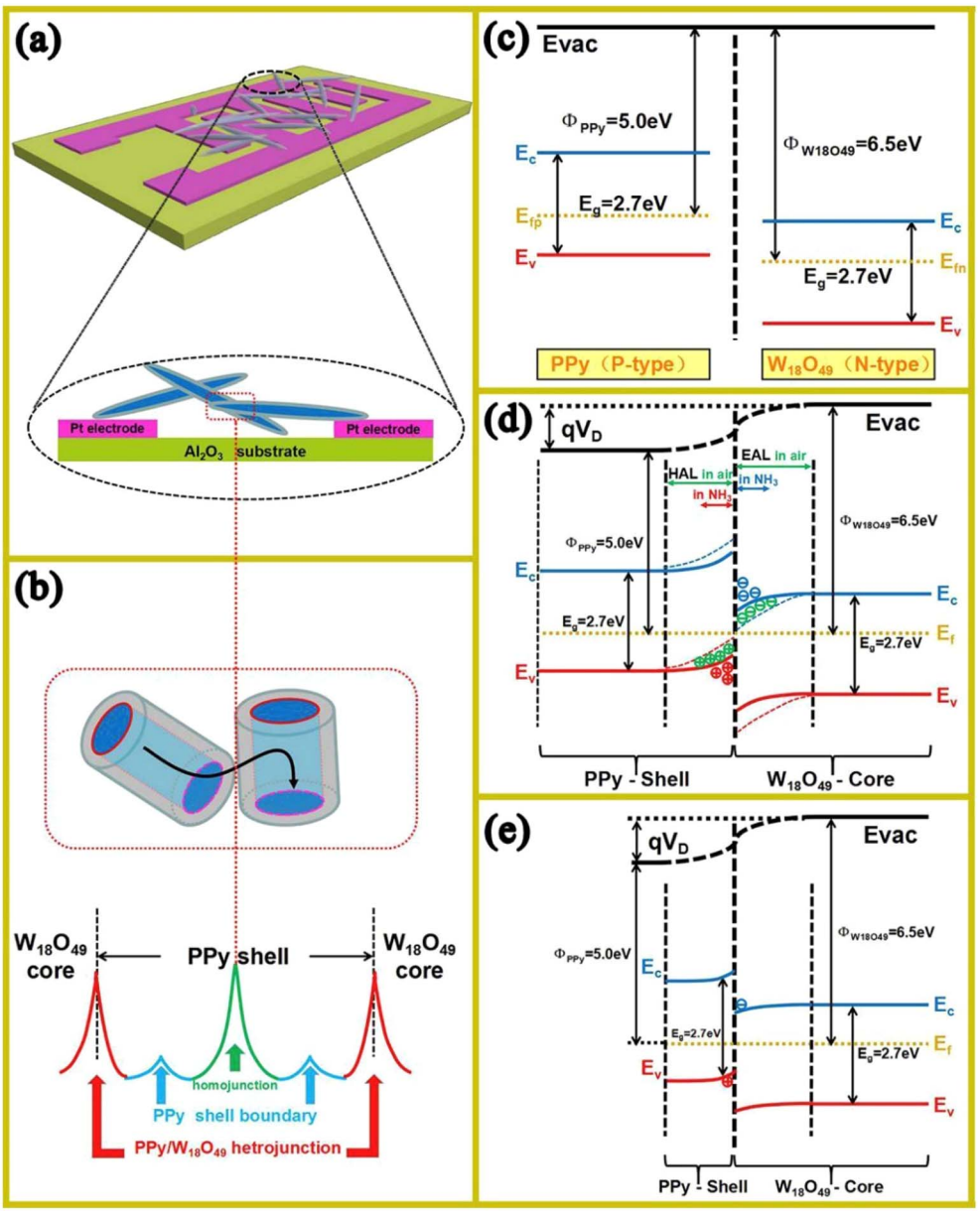

Fig. 17 (a) Schematic of the C–S NR sensor. (b) Various potential barriers in the PPy-$W_{18}O_{49}$ C–S NR sensor. (c) Energy band levels of the PPy-$W_{18}O_{49}$ C–S NRs before contact, (d) change in energy band upon exposure to NH_3 and (e) influence of thinner PPy shell on the energy levels.[99] Reproduced with permission from ref. 99. Copyright 2017, Elsevier.

significant adsorption of oxygen occurred due to (i) the presence of unstable surface states and (ii) catalytic activity of the TiO_2 shell. Hence, the EDL inside the shell significantly expanded and upward band bending occurred, causing the formation of an inversion layer, in which holes were the main charge carriers. Thereby, the sensors exhibited p-type behavior. The resistance of the sensor was determined by the presence of TiO_2–TiO_2 homojunctions, TiO_2–$W_{18}O_{49}$ heterojunctions and potential barriers as the grain boundaries of the TiO_2 shell. However, the effect of the grain boundary potential barrier was negligible in the thin shell layers. Fig. 18(b) and (c) exhibit the energy band levels of the $W_{18}O_{49}$–TiO_2 heterojunction before and after contact, respectively. The electron affinity, work function and band gap of TiO_2 are 4.6, and 4.7 eV, 3.6, and that of $W_{18}O_{49}$ are 6.5, 6.7 and 2.7 eV, respectively.[104] Thus, the electrons moved from TiO_2 to $W_{18}O_{49}$ to balance their Fermi levels, leading to the formation of heterojunctions at the interface of TiO_2 and $W_{18}O_{49}$ (Fig. 18(b)). In an NO_2 atmosphere, more electrons were extracted from the sensor, and the resistance increased.

Xiong *et al.*[105] synthesized a WO_3–$W_{18}O_{49}$ composite *via* a hydrothermal reaction at 200 °C for 24 h. Pristine $W_{18}O_{49}$ consisted of spindle-like particles (150–200 nm) (Fig. 19(a) and (c)), while the WO_3–$W_{18}O_{49}$ samples had a loose spindle-shaped structure composed of numerous well-aligned NWs with a diameter of 10–20 nm and length of 150–200 nm in (Fig. 19(b) and (d)), which were more suitable for gas adsorption.

The response (R_a/R_g) of WO_3–$W_{18}O_{49}$ was 23.3 to 500 ppm NH_3 at 250 °C, whereas the maximum response of the $W_{18}O_{49}$ sensor to 500 ppm NH_3 was ~5 at 200 °C. The selectivity of the composite sensor to NH_3 was related to the different optimal operating temperatures for gases. Given that the work functions of the two materials were different (Fig. 20(a)), in the contact areas and to match their Fermi levels, electrons moved from WO_3 to $W_{18}O_{49}$, resulting in band bending and the formation of an expanded depletion layer on WO_3 (Fig. 20(a) and (b)). Upon the injection of NH_3 gas and by release of electrons, the thickness of the EDL decreased, leading to a change in the resistance of the sensor. Secondly, the surface areas of WO_3–$W_{18}O_{49}$ and pristine $W_{18}O_{49}$ were ~95 and ~37 $m^2\ g^{-1}$, with pore volumes 0.2501 and 0.071 $cm^3\ g^{-1}$, respectively. Thus, the composite sensor offered a greater surface area and larger pores for gas molecules. Also, based on the XPS study, more oxygen ions were adsorbed on WO_3–$W_{18}O_{49}$ relative to the pristine $W_{18}O_{49}$, indicating the probability of higher reactions between them and gas molecules.

Hierarchical structures with a 3D morphology are very promising for the fabrication of gas sensors. In this regards, hierarchical WO_3 NS-$W_{18}O_{49}$ NW composites were prepared through the hydrothermal technique at 150 °C for 4 h using WCl_6 as the precursor, polyethylene–polypropylene glycol (P123) as the surfactant, and H_2O and ethanol as solvents.[106] In a fixed amount of ethanol (27.4 mL), WCl_6 (0.666 g) and P123 (0.167 g), depending on the amount of water, urchin-like $W_{18}O_{49}$ (no water), hierarchical $WO_3/W_{18}O_{49}$ (0.175 mL), and flower-like WO_3 (0.25 mL) were synthesized. The response (R_g/R_a) of the hierarchical $WO_3/W_{18}O_{49}$ to 1 ppm NO_2 gas was 1687

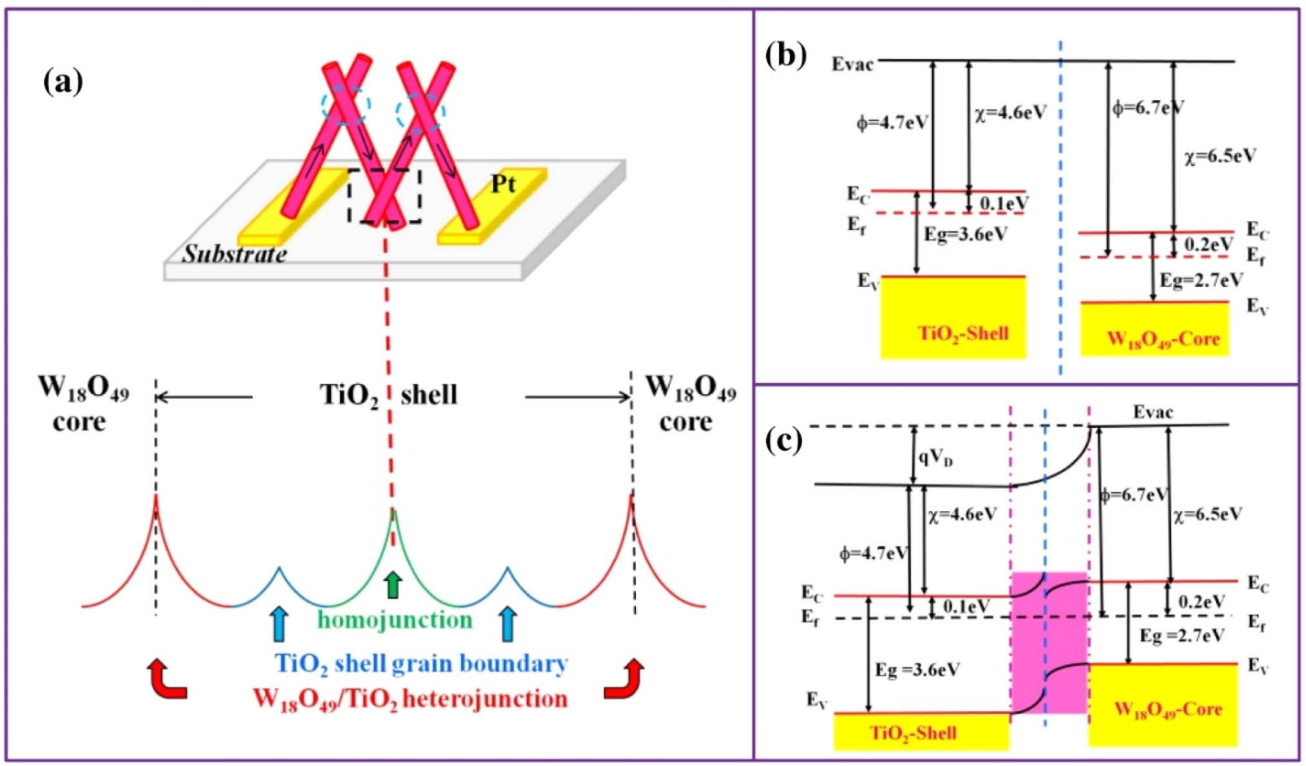

Fig. 18 (a) Schematic of the $W_{18}O_{49}/TiO_2$ C–S NW gas sensor mechanism. Energy band levels of the $W_{18}O_{49}/TiO_2$ C–S NW before (b) and after (c) contact.[101] Reproduced with permission from ref. 101. Copyright 2017, Elsevier.

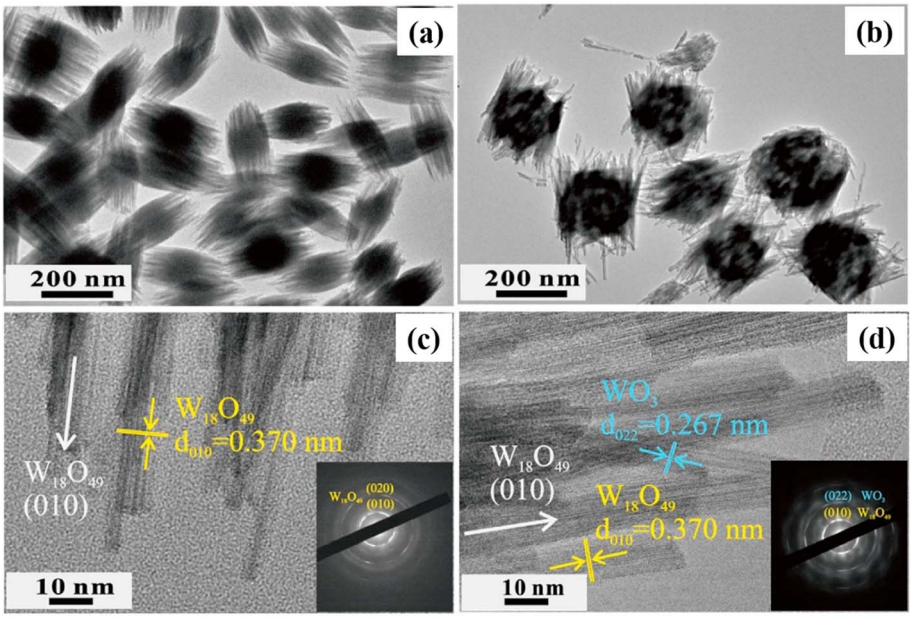

Fig. 19 TEM images of (a) the $W_{18}O_{49}$ and (b) WO_3–$W_{18}O_{49}$ composites and HRTEM images of (c) $W_{18}O_{49}$ and (d) WO_3–$W_{18}O_{49}$ composites (insets reveal the corresponding SAED patterns).[105] Reproduced with permission from ref. 105. Copyright 2018, Elsevier.

at 160 °C, which was much higher than that of the urchin-like $W_{18}O_{49}$ (826) and flower-like WO_3 (94). Furthermore, the t_{res} and t_{rec} of the hierarchical $WO_3/W_{18}O_{49}$ sensor were 36 s and 13 s, respectively. The fast dynamics of the sensor was related to the presence of abundant channels, leading to rapid diffusion and fast gas sensing reactions. Based on PL and electron paramagnetic resonance (EPR) studies, the sensors had almost the same amount of oxygen vacancies. Therefore, the difference between the sensing results was related to the synergistic nature of the NWs and NSs due to the fast electron separation and transport by the $W_{18}O_{49}$ NWs and abundant adsorption sites offered by the WO_3 NSs. Also, the NSs acted as a current collector, receiving electrons from the NWs to react with oxygen or NO_2 gas.

$W_{18}O_{49}$ NWs grown on SnO_2 NWs with hierarchical structures were prepared for sensing application. Initially SnO_2 NWs were grown *via* the vapor–liquid–solid (VLS) mechanism at 900 °C for 1 h. The SnO_2 NWs had diameters in the range of ~70–300 nm and lengths of ~5–100 μm. Next, $W_{18}O_{49}$ NWs with a diameter of ~50 nm and length of more than 2 μm were grown on the SnO_2 NWs *via* the thermal evaporation of W. The effect of the growth temperature (1850 °C and 2050 °C) and growth pressure (5×10^{-5} mbar and 7×10^{-4} mbar) on the nature of the $W_{18}O_{49}$ NWs was investigated. Given that higher pressure led to a higher oxidation rate and increased evaporation rate, the density, diameter and length of the $W_{18}O_{49}$ NWs increased with an increase in pressure. At a fixed pressure, an increase in temperature resulted in the same trend as mentioned above.

The single wire $SnO_2/W_{18}O_{49}$ heterojunction sensor revealed a response (I_g/I_a) of 11.0 to 6 ppm Cl_2 gas, while the t_{res} and t_{rec} were long, namely, 4.6 min and 17 min, respectively. Abnormally, the resistance decreased on exposure to Cl_2 gas which is an oxidizing gas. Based on the comparison of the sensing behavior of the networked wire and single wire gas sensors, it was reported that the grain boundaries had a normal response to Cl_2 gas, whereas the intragrain contribution was anomalous. Also, in the single wire gas sensor, the sensing reactions mainly occurred with lattice oxygen and oxygen adsorbed on its surface, resulting in an anomalous response, and additional sites for adsorption were not available due to the low defect density of the single wire gas sensor. The networked sensor had a large number of defect sites between the grains, on which additional Cl_2 was adsorbed, leading to a normal response to Cl_2.[107]

$W_{18}O_{49}$ hollow spheres were hydrothermally prepared at 180 °C for 16 h. Later, different amounts of $FeCl_3$ (0.01, 0.02, 0.04, and 0.06 g) were added to the $W_{18}O_{49}$ suspension and the mixed suspension was heated at 120 °C/1 h under hydrothermal conditions. After annealing at 400 °C for 2 h, the final $W_{18}O_{49}$-α-Fe_2O_3 composites with 3.99, 6.3, 13.98, and 18.98 wt% α-Fe_2O_3, were prepared.[108] The nanocomposites had a spherical hollow structure with an average diameter of ~450 nm. The hollow shells were thicker and solid after the addition of α-Fe_2O_3 to $W_{18}O_{49}$. However, the composite with the highest amount of α-Fe_2O_3 lost the hollow spherical morphology. The surface area of the $W_{18}O_{49}$ hollow spheres was 78 $m^2\ g^{-1}$, while that for the composite with 6.3 wt% α-Fe_2O_3 slightly decreased to 67 $m^2\ g^{-1}$ due to the coverage of the pores in the $W_{18}O_{49}$ hollow spheres. However, both samples showed a mesoporous nature, in which the target gas could penetrate the in-depth parts of the sensor easily (Fig. 21(a)–(c)). The sensor fabricated using the composite with 6.3 wt% α-Fe_2O_3 exhibited a response (R_a/R_g) of 5.61 to 100 ppm acetone at 260 °C, while the pristine sensor revealed a much lower response. Also, its t_{res} and t_{rec} were 10 and ~30 s, respectively. The selectivity to acetone was related to the oxygen-deficient nature of $W_{18}O_{49}$, where the W atoms in $W_{18}O_{49}$ had unsaturated coordination to oxygen, manifesting dangling

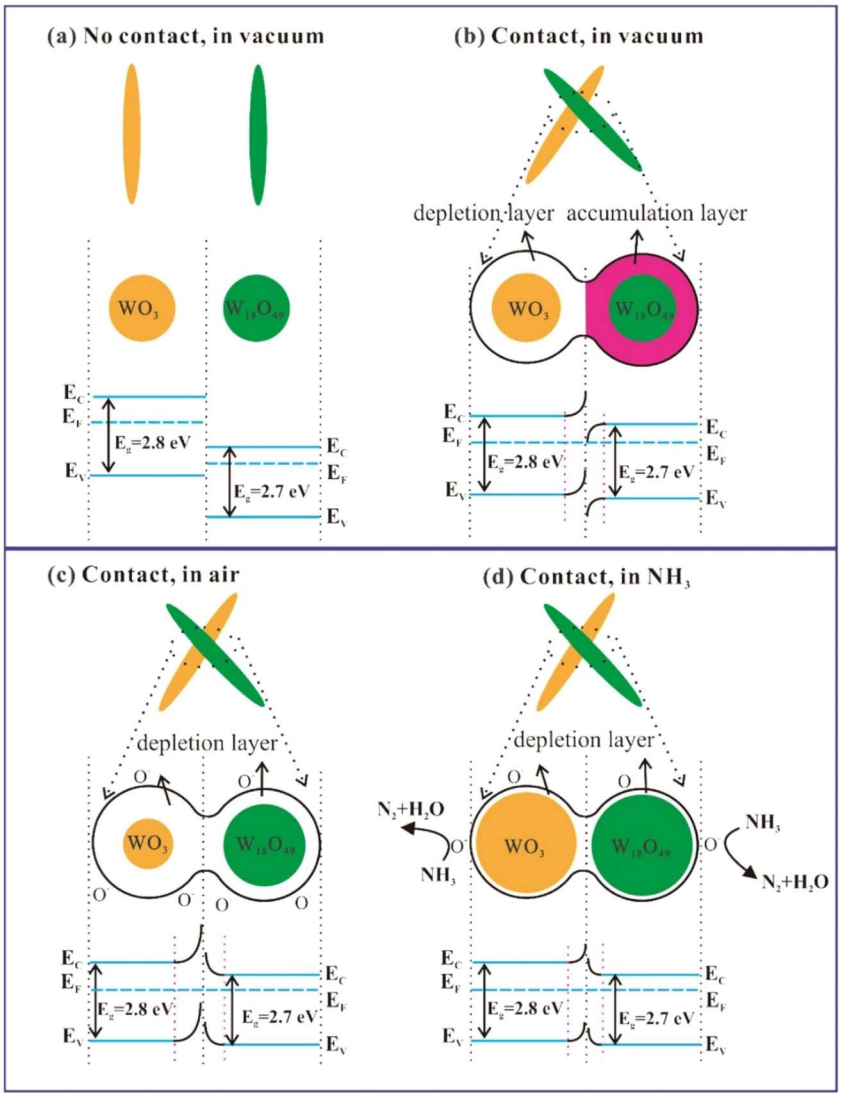

Fig. 20 Schematic of the energy band levels of WO_3 and $W_{18}O_{49}$ (a) before contact and after junction formation in (b) vacuum, (c) air and (d) NH_3 gas.[105] Reproduced with permission from ref. 105. Copyright 2018, Elsevier.

bonds and bringing about the highly polarized state of $W_{18}O_{49}$. Given that acetone has a larger dipole moment (2.88 D) than the interfering gases, it was easily adsorbed on the surface of $W_{18}O_{49}$. In air, the thickness of the EDL further increased because of the adsorption of chemisorbed oxygen species (Fig. 21(b)) and subsequent exposure to acetone decreased the thickness of the EDL (Fig. 21(c)). The creation of heterojunctions between different materials is one of the most powerful sources of resistance modulation in resistive gas sensors. Due to the difference in the work function of α-Fe_2O_3 (5.88 eV)[109] and $W_{18}O_{49}$ (4.6 eV) (Fig. 21(d)), electrons flowed from $W_{18}O_{49}$ to α-Fe_2O_3 to match the Fermi levels at both sides of the interfaces (Fig. 21(e)).

The effect of plasma treatment on the gas sensing features of $W_{18}O_{49}$ was investigated. Initially, $W_{18}O_{49}$ NWs were hydrothermally synthesized at 180 °C for 5 h. Then, some of the powder was treated with H_2 plasma at a fixed flow rate for 30 and 50 min, and the remaining powder was subjected to the same treatment conditions with Ar plasma. The 1D $W_{18}O_{49}$ along the (010) direction had accelerated anisotropic growth behavior, which provided surface defects as active sites for gas adsorption. Then, PANI with different thicknesses adjusted by amount of aniline monomer was applied on $W_{18}O_{49}$ *via* a chemical polymerization process. Oxygen vacancies were created at the interface of $W_{18}O_{49}$-PANI during plasma treatment, which acted as electron acceptors and promoted PANI to generate more protons to react with the target NH_3 (Fig. 22(a)).[110] Based on the EPR analysis, the concentration of oxygen vacancies in the Ar plasma-treated sample was lower than that in the H-plasma treated sample owing to their different atomic mass. Hence, Ar plasma could seriously destroy the surface lattice, resulting in the creation of various lattice defects, while the H_2 plasma mostly generated oxygen vacancies. The response (R_g/R_a) of the $W_{18}O_{49}$-PANI sensor after 50 min exposure to H_2 plasma was 35 to 100 ppm NH_3 at 25 °C, which was the highest response among the sensors. In fact, at

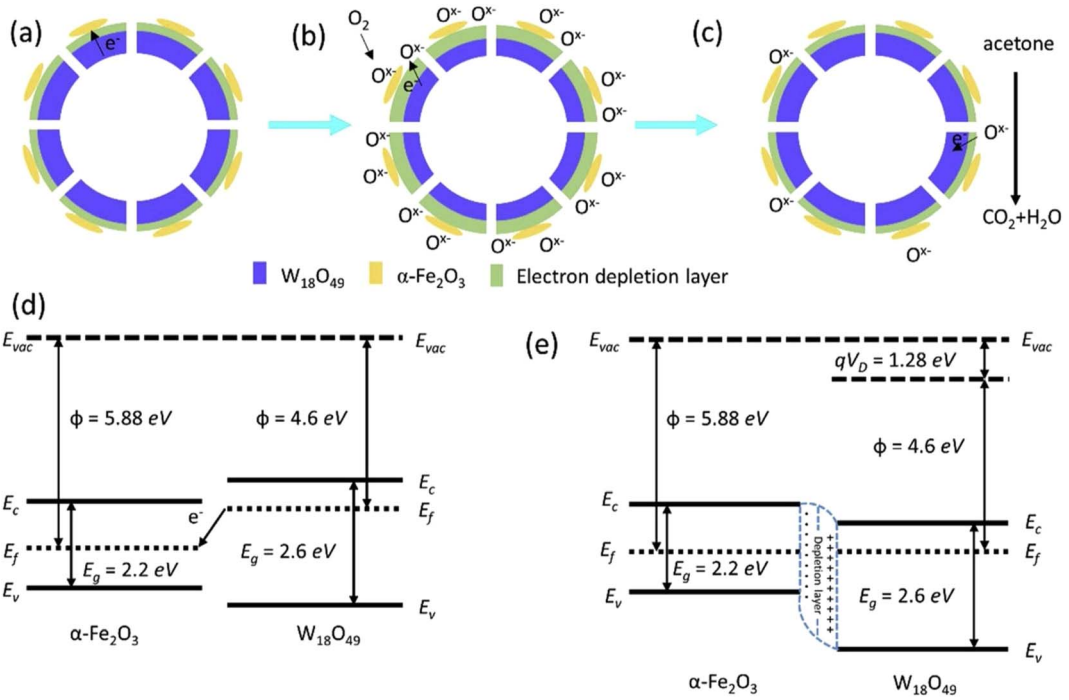

Fig. 21 Schematic of the $W_{18}O_{49}/\alpha$-Fe_2O_3 hollow sphere (a) in vacuum, (b) in air and (c) in acetone. (d and e) Energy band diagram of the $W_{18}O_{49}/\alpha$-Fe_2O_3 heterojunction before and after contact.[108] Reproduced with permission from ref. 108. Copyright 2019, Elsevier.

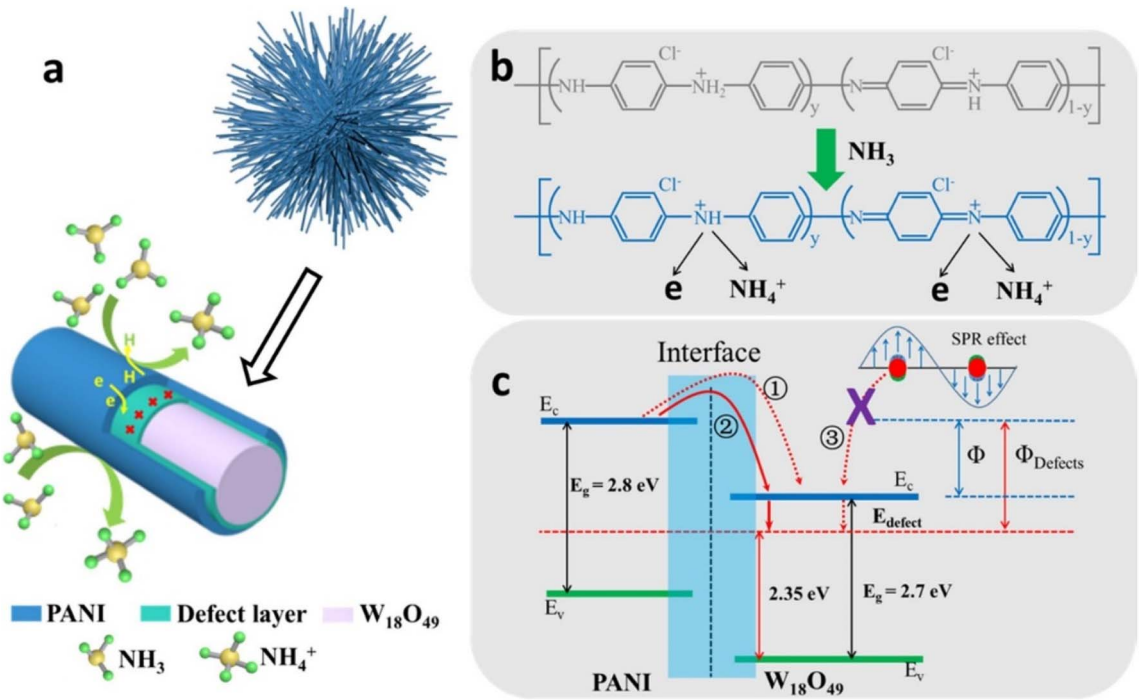

Fig. 22 (a) Schematic of $W_{18}O_{49}$-PANI C–S, (b) interaction of NH_3 molecules with PANI and (c) heterojunction band structure and electron flow paths.[110] Reproduced with permission from ref. 110. Copyright 2020, Elsevier.

a fixed plasma treatment time, the hydrogen plasma-treated sensor exhibited a better performance than the Ar-treated sensor due to the higher concentration of oxygen vacancies generated by hydrogen plasma treatment, consistent with another study.[111] Also with an increase in the plasma treatment time, the sensor showed a higher response due to the generation of more defects with longer times. At the same time, the H_2 plasma-treated sample had a better performance than the Ar

Table 1 Gas sensing performance of $W_{18}O_{49}$-based gas sensors

Sensing material	Synthesis method	Gas and	Conc. (ppm)	T (°C)	Response (R_a/R_g) or (R_g/R_a)	Ref.
Pristine sensors						
$W_{18}O_{49}$ nanoneedles	Solvothermal	NO_2	10	160	17	48
$W_{18}O_{49}$ NWs	Solvothermal	NH_3	45	RT	1.13 (I_a/I_g)	50
Single crystalline $W_{18}O_{49}$ NRs	Colloidal synthesis method	Ethanol	130	RT	3.5% $[\Delta R/R_a] \times 100$	52
$W_{18}O_{49}$ NWs	Chemical synthesis	Acetone	50	280	48.6	53
$W_{18}O_{49}$ mesocrystals	Solvothermal	NO_2	1	90	24.5	55
$W_{18}O_{49}$ NRs	Solvothermal	NO_2	5	150	131.5	57
$W_{18}O_{49}$ NWs	*In situ* oxidation of sputtered W layer	NO_2	1	150	4.4	59
Noble metal-decorated sensors						
Pd-decorated flower-like $W_{18}O_{49}$	Ultrasonic-solvothermal method	HCHO	15	180	25.1	61
Pd-decorated urchin-like $W_{18}O_{49}$	Hydrothermal and impregnation	H_2	1000	100	1600	63
Pt-decorated networked $W_{18}O_{49}$ NWs	Thermal evaporation and sputtering	H_2	1000	~48	1.6	65
Pt-decorated urchin-like $W_{18}O_{49}$ microstructures	Hydrothermal and chemical reduction	Ethanol	10	23	300	66
Pd@Au core–shell bimetallic NPs-decorated $W_{18}O_{49}$ NWs	Solvothermal and chemical reduction	H_2S	50	100	55.5	68
Au-decorated $Co_3O_4/W_{18}O_{49}$ hollow spheres	Hydrothermal and chemical reduction	TEA	2	270	16.7	69
Ag/AgCl-decorated $W_{18}O_{49}$ NRs	Solvothermal and UV reduction	H_2S	100	300	115.5	73
$Au_{39}Rh_{61}$-decorated urchin-like $W_{18}O_{49}$	Hydrothermal and co-precipitation	*n*-Butanol	50	260	11	75
Doped sensors						
Pd-doped $W_{18}O_{49}$ NWs	Hydrothermal	Acetone	50	175	146	81
Ni-doped rambutan-like $W_{18}O_{49}$	Solvothermal	*n*-Butanol	50	160	182	83
Co and Ni-doped porous $W_{18}O_{49}$ nano-urchins	Hydrothermal	TEA	50	250	114	86
0.6 at% Ti-doped $W_{18}O_{49}$ NWs	Hydrothermal	NO_2	4	25	23	88
Composite sensors						
$W_{18}O_{49}$/graphene nanocomposites	Hydrothermal	Ethanol	100	340	16.47	90
$WS_2/W_{18}O_{49}$ heterojunction	Pyrolysis of WO_3 in sulfur atmosphere	NH_3	5	RT	25.7% $[\Delta R/R_a] \times 100$	94
$W_{18}O_{49}/Ti_3C_2T_x$ MXene nanocomposite	Solvothermal	Acetone	20	300	11.6	96
PPy@$W_{18}O_{49}$ C–S NRs	Solvothermal and *in situ* polymerization	NH_3	20	15	4.1	100
$W_{18}O_{49}$–TiO_2 C–S NWs	Thermal oxidation and sputtering	NO_2	5	RT	36.5	101
WO_3–$W_{18}O_{49}$	Hydrothermal	NH_3	500	250	23.3	105
WO_3 NS-$W_{18}O_{49}$ NW composite	Hydrothermal	NO_2	1	160	1687	106
$SnO_2/W_{18}O_{49}$ heterojunction	VLS growth	Cl_2	6	RT	11 (I_g/I_a)	107
$W_{18}O_{49}$-α-Fe_2O_3 composite	Hydrothermal	Acetone	100	260	5.61	108
$W_{18}O_{49}$-PANI	Hydrothermal and *in situ* polymerization	NH_3	100	RT	35	109
$CeO_2/WO_{2.9}$ composite	Hydrothermal	*n*-Butanol	100	RT	23.68	115

plasma-treated sample, which may be due to the greater concentration of oxygen vacancies generated by the H_2 plasma treatment, in agreement with previous studies Also, the t_{rec} of the hydrogen plasma-treated sensor was shorter than that of the Ar plasma-treated sensor, which was again related to the presence of more oxygen defects in this sensor, accelerating the flow of electrons during the recovery period. Upon the interaction between PANI and NH_3 molecules, PANI lost an H atom, thus gaining an electron left by the H atom (Fig. 22(b)), causing the low response by the sensor. The free electrons were adsorbed by oxygen vacancies, permitting the occurrence of gas sensing reactions at a deeper level. Notably, due to the higher potential difference between the introduced oxygen vacancy energy level and the CB of PANI, the electron transfer in path 2 was more efficient than path 1 (Fig. 22(c)). Obviously, the presence of more oxygen vacancies in the hydrogen plasma-treated sensor led to better efficiency and a higher gas response.

7. Other sub-stoichiometric WO_{3-x} gas sensors

In comparison with $W_{18}O_{49}$, other sub-stoichiometric tungsten oxide nanostructures have been less studied for sensing purposes. Sub-stoichiometric $WO_{2.9}$ nanostructures have also been used for the detection of gases both experimentally and theoretically.[112,113] For example, Zhang *et al.*[114] prepared $WO_{2.9}$ flowers *via* the acid etching of W/Cu alloy powder. The sensor with the W/Cu ratio of 1/9 displayed an enhanced sensing performance to trimethylamine at 220 °C. The improved sensing output was related to the presence of high amounts of oxygen vacancies, a high surface area owing to its hierarchical flower structure and presence of energetic reaction sites on its surface. In another study,[115] button-shaped porous $CeO_2/WO_{2.9}$ composites with different amounts of Ce/W were synthesized *via* a hydrothermal reaction at 170 °C for 12 h. The optimal sensor displayed the highest response (R_a/R_g) of 23.68 to 100 ppm *n*-butanol at RT, which was related to the formation of double oxygen defects on the surface of the $CeO_2/WO_{2.9}$ heterostructure, the large surface area, and unique surface/interface conduction modes of the sensor. However, there are no reports on the fabrication of high-performance gas sensors based on $WO_{2.8}$ (W_5O_{14}). Overall, among the sub-stoichiometric WO_{3-x}, $W_{18}O_{49}$ is more favorable for sensing studies owing to its simple synthesis together with excellent semiconducting features.

Table 1 summarizes the gas sensing properties of the gas sensing performance of $W_{18}O_{49}$-based gas sensors. It can be seen that various toxic gases and VOCs can be detected by $W_{18}O_{49}$-based gas sensors. Also, their sensing temperatures are in the range of RT to 340 °C.

8. Conclusion and outlooks

Herein, the gas sensing characteristics of $W_{18}O_{49}$-based sensors were explained. There are various strategies for the synthesis of $W_{18}O_{49}$, among which the most common are hydrothermal synthesis and VLS growth. Hydrothermal synthesis has advantages such as the possibility of the synthesis of various morphologies, simple preparation procedures, and good control of the process variables such as temperature and time. However, generally it needs high synthesis pressures and long synthesis times. Alternatively, VLS growth is a simple synthesis method for the growth of 1D nanostructures such as NWs with good control of their diameters and length by control of the synthesis temperature and time. However, it often needs high temperatures for the growth of $W_{18}O_{49}$.

Pristine $W_{18}O_{49}$ gas sensors with various morphologies such as NWs have been successfully used for the detection of various toxic gases. However, their performance can be improved using different techniques such as doping, decoration with noble metals and composite formation. In all cases, optimization of the amount of added materials is required to achieve the highest sensing properties. Doping is often used with the addition of a small amount of metal cations into the $W_{18}O_{49}$ lattice. This results in the formation of structural defects and expansion or contraction of the lattice, which lead to changes in the surface and adsorption properties of doped $W_{18}O_{49}$. Decoration with noble metals such Pd, Pt and Au is another popular strategy to enhance the gas sensing features of $W_{18}O_{49}$ due to the catalytic and electronic effects of noble metals. Also, due to the catalytic effect of noble metals to some gases, the selectivity of $W_{18}O_{49}$ for a particular gas can be significantly increased. However, more studies are necessary to further explore the performance of $W_{18}O_{49}$ when it is decorated with noble metals. For example, no study related to Ag decoration on $W_{18}O_{49}$ has been reported to date. Another approach is bimetal decoration such as AuPt, AuPd, and PdPt on $W_{18}O_{49}$ to further increase its selectivity and response, owing to the synergistic effects of noble metals.

Composite formation is one the most reliable strategies to boost the sensing features of $W_{18}O_{49}$ because of the generation of a huge amount of heterojunctions at the interface areas of two different components. Composites of $W_{18}O_{49}$ with metal oxides, MXenes, TMDs and CPs have been reported for enhancing its gas sensing performance. Although MXenes, TMDs and CPs have lower sensing properties relative to metal oxides, they can work at lower temperatures, and therefore the sensing temperature of the fabricated sensors can be significantly decreased. In future works, composites of $W_{18}O_{49}$ with g-C_3N_4 and a combination of three sensing materials such as $W_{18}O_{49}$/TMD/MXene should be explored for gas sensing purposes.

Sensitivity is defined as the slope of the "response *versus* concentration" plot.[116] Obviously, a higher response to a certain concentration of gas will lead to higher sensitivity. $W_{18}O_{49}$ gas sensors have relatively good response and sensitivity. However, compared with SnO_2 and ZnO gas sensors, their performances are weaker. Also, a common shortage of resistance gas sensors is their poor selectivity. In this regards, $W_{18}O_{49}$ gas sensors also have poor selectivity to gases. However, their selectivity can be improved by noble metal decoration and formation of composites. The limit of detection is the minimum concentration of gas that can produce a sufficiently different resistance from the base resistance of a gas sensor.[117] Obviously, a lower

LOD is better for practical application. Unfortunately, most papers related to $W_{18}O_{49}$ gas sensors did not report the LOD of the fabricated sensors. In some cases, they can have an LOD in the range of ppb.

Often $W_{18}O_{49}$ gas sensors work at high temperatures, resulting in significant power consumption in the range of mW or W. This limits their applications in remote area or areas with energy shortage. Accordingly, in future studies, the power consumption of $W_{18}O_{49}$ sensors can be significantly decreased by (i) illumination of $W_{18}O_{49}$ with UV light during exposure to gas, (ii) employing of a gas sensor in self-heating mode by directly applying an external voltage to the sensor electrodes and generation of heat within the sensor and (iii) fabrication of single NW $W_{18}O_{49}$ gas sensor, which needs only negligible power for working at the sensing temperature.

Also, to increase the sensitivity of $W_{18}O_{49}$ sensors, irradiation with high energy beams including an electron beam or gamma rays can be applied to $W_{18}O_{49}$, resulting in the generation of defects. The created defects act as favorable sites for gas adsorption, resulting in an enhanced sensing response. Furthermore, the implantation of $W_{18}O_{49}$ by high energy ions not only generates structural defects in $W_{18}O_{49}$ but also simultaneously dope them in the $W_{18}O_{49}$ lattice. Another approach is to increase the SSA of $W_{18}O_{49}$ using the nanotube morphology or synthesis of highly porous morphologies derived from metal organic frameworks (MOFs). In particular, MOF-derived $W_{18}O_{49}$ has a highly porous structure, which allows the easy diffusion of gas molecules inside the sensing layer, resulting in a high response to gas.

Data availability

The data used to support the findings of this study are available from the corresponding author upon request.

Author contributions

M. Hjiri: formal analysis, writing and editing; I. Najeh: data curation; Fatemah M. Barakat: methodology; G. Neri: reviewing; supervision.

Ethical statement

All authors declare that the presented work was original research that has not been published previously, and not under consideration for publication elsewhere, in whole or in part.

Conflicts of interest

Authors have a responsibility to disclose interests that might appear to affect their ability to present data objectively. Readers will benefit from transparency, including knowing authors' and contributors' affiliations and interests. Sources of funding for research were disclosed.

Acknowledgements

This work was supported and funded by the Deanship of Scientific Research at Imam Mohammad Ibn Saud Islamic University (IMSIU) (grant number IMSIU-DDRSP2502).

References

1 A. Mirzaei, J.-H. Lee, S. M. Majhi, M. Weber, M. Bechelany, H. W. Kim and S. S. Kim, Resistive gas sensors based on metal-oxide nanowires, *J. Appl. Phys.*, 2019, **126**, 241102.
2 O. Bronte, F. García-García, D.-J. Lee, I. Urrutia, A. Uranga, M. Nieves, *et al.*, Impact of outdoor air pollution on severity and mortality in COVID-19 pneumonia, *Sci. Total Environ.*, 2023, **894**, 164877.
3 E. Merkus, Hold your breath! Air pollution and cognitive performance in Colombia, *World Dev. Sustainability*, 2024, **4**, 100123.
4 T. Wyttenbach and M. T. Bowers, Gas-phase conformations: the ion mobility/ion chromatography method, *Modern Mass Spectrom.*, 2003, **225**, 207–232.
5 K. D. Bartle and P. Myers, History of gas chromatography, *TrAC, Trends Anal. Chem.*, 2002, **21**, 547–557.
6 Z. Wang, L. Zhu, S. Sun, J. Wang and W. Yan, One-dimensional nanomaterials in resistive gas sensor: from material design to application, *Chemosensors*, 2021, **9**, 198.
7 A. Mirzaei and G. Neri, Microwave-assisted synthesis of metal oxide nanostructures for gas sensing application: a review, *Sens. Actuators, B*, 2016, **237**, 749–775.
8 J. Pu, Y. Gao, Q. Cao, G. Fu, X. Chen, Z. Pan and C. Guan, Vanadium metal-organic framework-derived multifunctional fibers for asymmetric supercapacitor, piezoresistive sensor, and electrochemical water splitting, *SmartMat*, 2022, **3**, 608–618.
9 B. Guruprasad and M. Shwetha, Design and fabrication of cantilever MEMS sensor model for electro-chemical gas sensor, *Int. J. Eng. Res. Technol.*, 2020, **9**, 704–715.
10 S. Okazaki, H. Kawada, Y. Koshiba, N. Kasai, Y. Maru, T. Mizutani, *et al.*, Catalytic combustion type optical fiber Bragg grating hydrogen gas sensor using platinum-loaded fumed silica powder, *Int. J. Hydrogen Energy*, 2023, **48**, 9512–9527.
11 E. L. Gardner, J. W. Gardner and F. Udrea, Micromachined thermal gas sensors—A review, *Sensors*, 2023, **23**, 681.
12 Y. Li, L. Yu, C. Zheng, Z. Ma, S. Yang, F. Song, *et al.*, Development and field deployment of a mid-infrared CO and CO_2 dual-gas sensor system for early fire detection and location, *Spectrochim. Acta, Part A*, 2022, **270**, 120834.
13 M. Bonyani, S. M. Zebarjad, K. Janghorban, J.-Y. Kim, H. W. Kim and S. S. Kim, Enhanced NO_2 gas sensing properties of ZnO-PANI composite nanofibers, *Ceram. Int.*, 2023, **49**, 1238–1249.
14 N. Kaur, M. Singh and E. Comini, One-dimensional nanostructured oxide chemoresistive sensors, *Langmuir*, 2020, **36**, 6326–6344.
15 M. Bonyani, S. M. Zebarjad, K. Janghorban, J.-Y. Kim, H. W. Kim and S. S. Kim, Au-decorated polyaniline-ZnO

electrospun composite nanofiber gas sensors with enhanced response to NO_2 gas, *Chemosensors*, 2022, **10**, 388.

16 M. Bonyani, S. M. Zebarjad, K. Janghorban, J.-Y. Kim, H. W. Kim and S. S. Kim, Au sputter-deposited ZnO nanofibers with enhanced NO_2 gas response, *Sens. Actuators, B*, 2022, **372**, 132636.

17 A. Mirzaei, Z. Kordrostami, M. Shahbaz, J.-Y. Kim, H. W. Kim and S. S. Kim, Resistive-based gas sensors using quantum dots: a review, *Sensors*, 2022, **22**, 4369.

18 H.-J. Kim and J.-H. Lee, Highly sensitive and selective gas sensors using p-type oxide semiconductors: overview, *Sens. Actuators, B*, 2014, **192**, 607–627.

19 N. Yamazoe, G. Sakai and K. Shimanoe, Oxide semiconductor gas sensors, *Catal. Surv. Asia*, 2003, **7**, 63–75.

20 J. Walker, P. Karnati, S. A. Akbar and P. A. Morris, Selectivity mechanisms in resistive-type metal oxide heterostructural gas sensors, *Sens. Actuators, B*, 2022, **355**, 131242.

21 J. H. Lee, J. Y. Kim, A. Mirzaei, H. W. Kim and S. S. Kim, Significant enhancement of hydrogen-sensing properties of ZnO nanofibers through NiO loading, *Nanomaterials*, 2018, **8**, 902.

22 Y. Jian, W. Hu, Z. Zhao, P. Cheng, H. Haick, M. Yao and W. Wu, Gas sensors based on chemi-resistive hybrid functional nanomaterials, *Nano-Micro Lett.*, 2020, **12**, 1–43.

23 M. D. El-Muraikhi, A. I. Ayesh and A. Mirzaei, Resistive gas sensors based on inorganic nanotubes: a review, *J. Alloys Compd.*, 2025, **1020**, 179585.

24 M. Zhang, C. Yang, Z. Zhang, W. Tian, B. Hui, J. Zhang and K. Zhang, Tungsten oxide polymorphs and their multifunctional applications, *Adv. Colloid Interface Sci.*, 2022, **300**, 102596.

25 Y. Qiu, Y. Wang and C. Song, Facile synthesis of $W_{18}O_{49}$/graphene nanocomposites for highly sensitive ethanol gas sensors, *Colloids Surf., A*, 2021, **616**, 126300.

26 M. Saqib, J. Jelenc, L. Pirker, S. D. Škapin, L. D. Pietro, U. Ramsperger, *et al.*, Field emission properties of single crystalline W_5O_{14} and $W_{18}O_{49}$ nanowires, *J. Electron Spectrosc. Relat. Phenom.*, 2020, **241**, 146837.

27 F. R. Sale, Heat capacities of the tungsten oxides WO_3, $W_{20}O_{58}$, $W_{18}O_{49}$ and WO_2, *Thermochim. Acta*, 1979, **30**, 163–171.

28 P. Bhavani, K.-J. J. D. Praveen Kumar, M. Hussain and Y.-K. Park, Recent advances in wide solar spectrum active $W_{18}O_{49}$-based photocatalysts for energy and environmental applications, *Catal. Rev.*, 2023, **65**, 1521–1566.

29 S. J. Park, S. M. Lee, J. Lee, S. Choi, G. B. Nam, Y. K. Jo, I. S. Hwang and H. W. Jang, Pd-$W_{18}O_{49}$ nanowire MEMS gas sensor for ultraselective dual detection of hydrogen and ammonia, *Small*, 2025, **21**, 2405809.

30 Z. Huang, J. Song, L. Pan, X. Zhang, L. Wang and J. Zou, Tungsten oxides for photocatalysis, electrochemistry, and phototherapy, *Adv. Mater.*, 2015, **27**, 5309–5327.

31 H. Gu, C. Guo, S. Zhang, L. Bi, T. Li, T. Sun, *et al.*, Highly efficient, near-infrared and visible light modulated electrochromic devices based on polyoxometalates and $W_{18}O_{49}$ nanowires, *ACS Nano*, 2018, **12**, 559–567.

32 S. Sui, Y. Liao, Y. Xie, X. Wang, L. Li, Z. Luo, *et al.*, High catalytic activity of $W_{18}O_{49}$ nanowire-reduced graphite oxide composite counter electrode for dye-sensitized solar cells, *ChemistrySelect*, 2017, **2**, 8927–8935.

33 Z. Zhang, J. Liang, K. Liu, W. Tian, X. Liang, K. Zhao and K. Zhang, Defect-engineered WO_{3-x} architectures coupled with random forest algorithm enables real-time seafood quality assessment, *ACS Sens.*, 2024, **9**, 4196–4206.

34 W. Ding, X. Wang, C. Yang, P. Wang, W. Tian, K. Zhao and K. Zhang, Interfacial photo-reduction of graphene oxide on defective WO_{3-x} for multifunctional applications in sensor, catalyst and supercapacitor, *Appl. Surf. Sci.*, 2022, **606**, 154877.

35 W. Ding, M. Feng, Z. Zhang, F. Fan, L. Chen and K. Zhang, Machine learning-motivated trace triethylamine identification by bismuth vanadate/tungsten oxide heterostructures, *J. Colloid Interface Sci.*, 2025, **682**, 1140–1150.

36 Z. Zou, Z. Zhao, Z. Zhang, W. Tian, C. Yang, X. Jin and K. Zhang, Room-temperature optoelectronic gas sensor based on core–shell g-C_3N_4@WO_3 heterocomposites for efficient ammonia detection, *Anal. Chem.*, 2023, **95**, 2110–2118.

37 M. Zhang, K. Liu, X. Zhang, B. Wang, X. Xu, X. Du, C. Yang and K. Zhang, Interfacial energy barrier tuning of hierarchical Bi_2O_3/WO_3 heterojunctions for advanced triethylamine sensor, *J. Adv. Ceram.*, 2022, **11**, 1860–1872.

38 M. Zhang, Z. Zhao, B. Hui, J. Sun, J. Sun, W. Tian, Z. Zhang, K. Zhang and Y. Xia, Carbonized polymer dots activated hierarchical tungsten oxide for efficient and stable triethylamine sensor, *J. Hazard. Mater.*, 2021, **416**, 126161.

39 N.-F. Yan, H.-M. Cui, J.-S. Shi, S.-Y. You and S. Liu, Recent progress of $W_{18}O_{49}$ nanowires for energy conversion and storage, *Tungsten*, 2023, **5**, 371–390.

40 P. Zhao, S. Ren, Y. Liu, W. Huang, C. Zhang and J. He, PL–$W_{18}O_{49}$–TPZ nanoparticles for simultaneous hypoxia-activated chemotherapy and photothermal therapy, *ACS Appl. Mater. Interfaces*, 2018, **10**, 3405–3413.

41 J. Jung and D. H. Kim, $W_{18}O_{49}$ nanowires assembled on carbon felt for application to supercapacitors, *Appl. Surf. Sci.*, 2018, **433**, 750–755.

42 P. Zheng, Y. Ami'erjiang, B. Liu, M. Wang, H. Ding, B. Ding, *et al.*, Oxygen-vacancy-engineered $W_{18}O_{49-x}$ nanobrush with a suitable band structure for highly efficient sonodynamic therapy, *Angew. Chem., Int. Ed.*, 2024, e202317218.

43 S. Li, J. Liu, W. Su, Y. Wang, J. Li, C. Ning, J. Ren, X. Wen, W. Zhang, Y. Tong and C. Wang, Tuning excited-state electronic structure in tungsten oxide for enhanced nitrogen photooxidation as fertilizer, *Appl. Catal., B*, 2024, **343**, 123539.

44 Z. Zhou, R. Tang, L. Li, S. Xiong, H. Zeng, J. Zheng, *et al.*, $W_{18}O_{49}$-based photocatalyst: enhanced strategies for photocatalysis employment, *Sep. Purif. Technol.*, 2023, **12**, 4028.

45 A. Sharma, S. B. Eadi, H. Noothalapati, M. Otyepka, H. D. Lee and K. Jayaramulu, Porous materials as effective chemiresistive gas sensors, *Chem. Soc. Rev.*, 2024, **53**, 2530–2577.

46 L. Y. Zhu, L. X. Ou, L. W. Mao, X. Y. Wu, Y. P. Liu and H. L. Lu, Advances in noble metal-decorated metal oxide nanomaterials for chemiresistive gas sensors: overview, *Nano-Micro Lett.*, 2023, **15**, 89.

47 R. Diehl, G. Brandt and E. Salje, The crystal structure of triclinic WO_3, *Acta Crystallogr., Sect. B*, 1978, **34**, 1105–1111.

48 Y. Qiu and Y. Wang, Controllable synthesis of $W_{18}O_{49}$ nanoneedles for high-performance NO_2 gas sensors, *J. Alloys Compd.*, 2023, **944**, 169199.

49 D. Kwak, Y. Lei and R. Maric, Ammonia gas sensors: a comprehensive review, *Talanta*, 2019, **204**, 713–730.

50 Y. Zhao and Y. Zhu, Room temperature ammonia sensing properties of $W_{18}O_{49}$ nanowires, *Sens. Actuators, B*, 2009, **137**, 27–31.

51 A. Mirzaei, S. G. Leonardi and G. Neri, Detection of hazardous volatile organic compounds (VOCs) by metal oxide nanostructures-based gas sensors: a review, *Ceram. Int.*, 2016, **42**, 15119–15141.

52 Y. S. Kim and K. Lee, Material and gas-sensing properties of tungsten oxide nanorod thin-films, *J. Nanosci. Nanotechnol.*, 2009, **9**, 2463–2468.

53 W. Zhang, Y. Fan, T. Yuan, B. Lu, Y. Liu, Z. Li, *et al.*, Ultrafine tungsten oxide nanowires: synthesis and highly selective acetone sensing and mechanism analysis, *ACS Appl. Mater. Interfaces*, 2020, **12**, 3755–3763.

54 L. Bahrig, S. G. Hickey and A. Eychmüller, Mesocrystalline materials and the involvement of oriented attachment – a review, *CrystEngComm*, 2014, **16**, 9408–9424.

55 D. Wang, J. Sun, X. Cao, Y. Zhu, Q. Wang, G. Wang, *et al.*, High-performance gas sensing achieved by mesoporous tungsten oxide mesocrystals with increased oxygen vacancies, *J. Mater. Chem. A*, 2013, **1**, 8653–8657.

56 Y. Cui and C. M. Lieber, Functional nanoscale electronic devices assembled using silicon nanowire building blocks, *Science*, 2001, **291**, 851–853.

57 Y. Qin, X. Li, F. Wang and M. Hu, Solvothermally synthesized tungsten oxide nanowires/nanorods for NO_2 gas sensor applications, *J. Alloys Compd.*, 2011, **509**, 8401–8406.

58 G. Gu, B. Zheng, W. Q. Han, S. Roth and J. Liu, Tungsten oxide nanowires on tungsten substrates, *Nano Lett.*, 2002, **2**, 849–851.

59 Y. Qin, W. Xie, Y. Liu and Z. Ye, Thermal-oxidative growth of aligned $W_{18}O_{49}$ nanowire arrays for high performance gas sensor, *Sens. Actuators, B*, 2016, **223**, 487–495.

60 S. Navale, M. Shahbaz, A. Mirzaei, S. S. Kim and H. W. Kim, Effect of Ag addition on the gas-sensing properties of nanostructured resistive-based gas sensors: an overview, *Sensors*, 2021, **21**, 6454.

61 P. Wang, S. Guo, Z. Hu, T. Li, S. Pu, H. Mao, *et al.*, $W_{18}O_{49}$ sensitized with Pd nanoparticles for ultrasensitive ppb-level formaldehyde detection, *Chem. Eng. J.*, 2023, **456**, 140988.

62 J.-H. Kim, A. Mirzaei, H. W. Kim, P. Wu and S. S. Kim, Design of supersensitive and selective ZnO-nanofiber-based sensors for H_2 gas sensing by electron-beam irradiation, *Sens. Actuators, B*, 2019, **293**, 210–223.

63 R. Zhou, X. Lin, D. Xue, F. Zong, J. Zhang, X. Duan, *et al.*, Enhanced H_2 gas sensing properties by Pd-loaded urchin-like $W_{18}O_{49}$ hierarchical nanostructures, *Sens. Actuators, B*, 2018, **260**, 900–907.

64 A. Kolmakov, D. Klenov, Y. Lilach, S. Stemmer and M. Moskovits, Enhanced gas sensing by individual SnO_2 nanowires and nanobelts functionalized with Pd catalyst particles, *Nano Lett.*, 2005, **5**, 667–673.

65 L. F. Zhu, J. C. She, J. Y. Luo, S. Z. Deng, J. Chen, X. W. Ji, *et al.*, Self-heated hydrogen gas sensors based on Pt-coated $W_{18}O_{49}$ nanowire networks with high sensitivity, good selectivity and low power consumption, *Sens. Actuators, B*, 2011, **153**, 354–360.

66 Y. Ou, G. Zhu, W. Zhang, S. Zhang, J. Gao, H. Lu, *et al.*, Achieving rapid response and high sensitivity in ethanol gas sensing using a Pt/$W_{18}O_{49}$ ohmic contact *via* modulating the adsorption and activation properties: Theoretical and experimental insights, *Sens. Actuators, B*, 2021, **347**, 130601.

67 X. Xiao, X. Zhou, J. Ma, Y. Zhu, X. Cheng, W. Luo, *et al.*, Rational synthesis and gas sensing performance of ordered mesoporous semiconducting WO_3/NiO composites, *ACS Appl. Mater. Interfaces*, 2019, **11**, 26268–26276.

68 W. Zhang, T. Yuan, X. Wang, Z. Cheng and J. Xu, Coal mine gases sensors with dual selectivity at variable temperatures based on a $W_{18}O_{49}$ ultra-fine nanowires/Pd@ Au bimetallic nanoparticles composite, *Sens. Actuators, B*, 2022, **354**, 131004.

69 L. Yu, X. Y. Yu and X. W. Lou, The design and synthesis of hollow micro-/nanostructures: present and future trends, *Adv. Mater.*, 2018, **30**, 1800939.

70 Y. Xu, T. Ma, L. Zheng, L. Sun, X. Liu, Y. Zhao, *et al.*, Rational design of Au/Co_3O_4-functionalized $W_{18}O_{49}$ hollow heterostructures with high sensitivity and ultralow limit for triethylamine detection, *Sens. Actuators, B*, 2019, **284**, 202–212.

71 X. Wang, J. I. Feng, Y. Bai, Q. Zhang and Y. Yin, Synthesis, properties, and applications of hollow micro-/nanostructures, *Chem. Rev.*, 2016, **116**, 10983–11060.

72 Y. Wang, F. Liu, H. Yuan and T. Hu, Interface engineering of Co_3O_4—$SmMn_2O_5$ nanosheets for efficient oxygen reduction electrocatalysis, *Front. Mater. Sci.*, 2021, **15**, 567–576.

73 S. Sun, X. Chang, L. Dong, Y. Zhang, Z. Li and Y. Qiu, $W_{18}O_{49}$ nanorods decorated with Ag/AgCl nanoparticles as highly-sensitive gas-sensing material and visible-light-driven photocatalyst, *J. Solid State Chem.*, 2011, **184**, 2190–2195.

74 N. Yamazoe, New approaches for improving semiconductor gas sensors, *Sens. Actuators, B*, 1991, **5**, 7–19.

75 J. Bai, Y. Li, Y. Liu, H. Wang, F. Liu, F. Liu, *et al.*, $Au_{39}Rh_{61}$ alloy nanocrystal-decorated $W_{18}O_{49}$ for enhanced detection of *n*-butanol, *ACS Sens.*, 2019, **4**, 2662–2670.

76 R. Xing, Q. Li, L. Xia, J. Song, L. Xu, J. Zhang, *et al.*, Au-modified three-dimensional In_2O_3 inverse opals: synthesis and improved performance for acetone sensing toward diagnosis of diabetes, *Nanoscale*, 2015, **7**, 13051–13060.

77 V. Amiri, H. Roshan, A. Mirzaei, G. Neri and A. I. Ayesh, Nanostructured metal oxide-based acetone gas sensors: a review, *Sensors*, 2020, **20**, 3096.

78 C. Wang, Y. Li, F. Gong, Y. Zhang, S. Fang and H. Zhang, Advances in doped ZnO nanostructures for gas sensor, *Chem. Rec.*, 2020, **20**, 1553–1567.

79 N. Zhang, A. Jalil, D. Wu, S. Chen, Y. Liu, C. Gao, *et al.*, Refining defect states in $W_{18}O_{49}$ by Mo doping: a strategy for tuning N_2 activation towards solar-driven nitrogen fixation, *J. Am. Chem. Soc.*, 2018, **140**, 9434–9443.

80 X. Zhong, Y. Sun, X. Chen, G. Zhuang, X. Li and J. Wang, Mo doping induced more active sites in urchin-like $W_{18}O_{49}$ nanostructure with remarkably enhanced performance for hydrogen evolution reaction, *Adv. Funct. Mater.*, 2016, **26**, 5778–5786.

81 P. Li, Z. Zhang, Z. Zhuang, J. Guo, Z. Fang, S. L. Fereja, *et al.*, Pd-doping-induced oxygen vacancies in one-dimensional tungsten oxide nanowires for enhanced acetone gas sensing, *Anal. Chem.*, 2021, **93**, 7465–7472.

82 Z. Liu, B. Liu, W. Xie, H. Li, R. Zhou, Q. Li, *et al.*, Enhanced selective acetone sensing characteristics based on Co-doped WO_3 hierarchical flower-like nanostructures assembled with nanoplates, *Sens. Actuators, B*, 2016, **235**, 614–621.

83 R. Wu, S.-Q. Guo, Y.-C. Li, M.-Y. Qi, B. Ge and J.-M. Song, Improving the sensing performance of rambutan-like $W_{18}O_{49}$ based gas sensor for *n*-butanol by Ni doping, *Sens. Actuators, B*, 2024, **410**, 135671.

84 G. Li, Z. Cheng, Q. Xiang, L. Yan, X. Wang and J. Xu, Bimetal PdAu decorated SnO_2 nanosheets based gas sensor with temperature-dependent dual selectivity for detecting formaldehyde and acetone, *Sens. Actuators, B*, 2019, **283**, 590–601.

85 S. Zeb, Z. Yang, R. Hu, M. Umair, S. Naz, Y. Cui, *et al.*, Electronic structure and oxygen vacancy tuning of Co & Ni co-doped $W_{18}O_{49}$ nanourchins for efficient TEA gas sensing, *Chem. Eng. J.*, 2023, **465**, 142815.

86 M. Shi, X. Tong, W. Li, J. Fang, L. Chen and C. Ma, Enhanced electrocatalytic oxygen reduction on $NiWO_x$ solid solution with induced oxygen defects, *ACS Appl. Mater. Interfaces*, 2017, **9**, 34990–35000.

87 H. Xu, R. Hu, Y. Zhang, H. Yan, Q. Zhu, J. Shang, *et al.*, Nano high-entropy alloy with strong affinity driving fast polysulfide conversion towards stable lithium sulfur batteries, *Energy Storage Mater.*, 2021, **43**, 212–220.

88 Y. Qin, X. Sun, X. Li and M. Hu, Room temperature NO_2-sensing properties of Ti-added nonstoichiometric tungsten oxide nanowires, *Sens. Actuators, B*, 2012, **162**, 244–250.

89 A. R. Urade, I. Lahiri and K. S. Suresh, Graphene properties, synthesis and applications: a review, *JOM*, 2023, **75**, 614–630.

90 Y. Qiu, Y. Wang and C. Song, Facile synthesis of $W_{18}O_{49}$/graphene nanocomposites for highly sensitive ethanol gas sensors, *Colloids Surf., A*, 2021, **616**, 126300.

91 J.-H. Kim, A. Mirzaei, Y. Zheng, J.-H. Lee, J.-Y. Kim, H. W. Kim, *et al.*, Enhancement of H_2S sensing performance of p-CuO nanofibers by loading p-reduced graphene oxide nanosheets, *Sens. Actuators, B*, 2019, **281**, 453–461.

92 H. W. Kim, Y. J. Kwon, A. Mirzaei, S. Y. Kang, M. S. Choi, J. H. Bang, *et al.*, Synthesis of zinc oxide semiconductors-graphene nanocomposites by microwave irradiation for application to gas sensors, *Sens. Actuators, B*, 2017, **249**, 590–601.

93 W. Zheng, X. Liu, J. Xie, G. Lu and J. Zhang, Emerging van der Waals junctions based on TMDs materials for advanced gas sensors, *Coord. Chem. Rev.*, 2021, **447**, 214151.

94 M. Manoharan, K. Govindharaj, K. Muthumalai, R. Pandian, Y. Haldorai and R. T. Rajendra Kumar, Highly selective room temperature detection of NH_3 and NO_x using oxygen-deficient $W_{18}O_{49}$-supported WS_2 heterojunctions, *ACS Appl. Mater. Interfaces*, 2023, **15**, 4703–4712.

95 A. Mirzaei, M. H. Lee, H. Safaeian, T.-U. Kim, J.-Y. Kim, H. W. Kim, *et al.*, Room temperature chemiresistive gas sensors based on 2D MXenes, *Sensors*, 2023, **23**, 8829.

96 S. Sun, M. Wang, X. Chang, Y. Jiang, D. Zhang, D. Wang, *et al.*, $W_{18}O_{49}/Ti_3C_2T_x$ Mxene nanocomposites for highly sensitive acetone gas sensor with low detection limit, *Sens. Actuators, B*, 2020, **304**, 127274.

97 W. Li, Y. Liu, X. Lu, Y. Huang, Y. Liu, S. Cheng, *et al.*, A cross-sectional study of breath acetone based on diabetic metabolic disorders, *J. Breath Res.*, 2015, **9**, 016005.

98 V. Kumar, A. Mirzaei, M. Bonyani, K.-H. Kim, H. W. Kim and S. S. Kim, Advances in electrospun nanofiber fabrication for polyaniline (PANI)-based chemoresistive sensors for gaseous ammonia, *TrAC, Trends Anal. Chem.*, 2020, **129**, 115938.

99 Y. Qin, T. Zhang and Z. Cui, Core-shell structure of polypyrrole grown on $W_{18}O_{49}$ nanorods for high performance gas sensor operating at room temperature, *Org. Electron.*, 2017, **48**, 254–261.

100 Y. Xiong, W. Xu, D. Ding, W. Lu, L. Zhu, Z. Zhu, *et al.*, Ultra-sensitive NH_3 sensor based on flower-shaped SnS_2 nanostructures with sub-ppm detection ability, *J. Hazard. Mater.*, 2018, **341**, 159–167.

101 Y. Qin, X. Zhang, Y. Wang and Y. Liu, Remarkable improvement of $W_{18}O_{49}/TiO_2$ heteronanowires in ambient temperature-responsive NO_2-sensing abilities and its unexpected np transition phenomenon, *Sens. Actuators, B*, 2017, **240**, 477–486.

102 C. Zhang, M. Debliquy, A. Boudiba, H. Liao and C. Coddet, Sensing properties of atmospheric plasma-sprayed WO_3 coating for sub-ppm NO_2 detection, *Sens. Actuators, B*, 2010, **144**, 280–288.

103 S. Vallejos, T. Stoycheva, P. Umek, C. Navio, R. Snyders and C. Bittencourt, Au nanoparticle-functionalised WO_3 nanoneedles and their application in high sensitivity gas sensor devices, *Chem. Commun.*, 2011, **47**, 565–567.

104 Y. Zhuo, L. Huang, Y. Ling, H. Li and J. Wang, A novel NO_2 sensor based on TiO_2 nanotubes array with in-situ Au decoration, *J. Nanosci. Nanotechnol.*, 2013, **13**, 1177–1181.

105 Y. Xiong, Z. Zhu, T. Guo, H. Li and Q. Xue, Synthesis of nanowire bundle-like WO_3-$W_{18}O_{49}$ heterostructures for highly sensitive NH_3 sensor application, *J. Hazard. Mater.*, 2018, **353**, 290–299.

106 B.-R. Wang, R.-Z. Wang, L.-Y. Liu, C. Wang, Y.-F. Zhang and J.-B. Sun, WO_3 nanosheet/$W_{18}O_{49}$ nanowire composites for NO_2 sensing, *ACS Appl. Nano Mater.*, 2020, **3**, 5473–5480.

107 S. Sen, P. Kanitkar, A. Sharma, K. P. Muthe, A. Rath, S. K. Deshpande, *et al.*, Growth of SnO_2/$W_{18}O_{49}$ nanowire hierarchical heterostructure and their application as chemical sensor, *Sens. Actuators, B*, 2010, **147**, 453–460.

108 Y. Xu, T. Ma, L. Zheng, Y. Zhao, X. Liu and J. Zhang, Heterostructures of hematite-sensitized $W_{18}O_{49}$ hollow spheres for improved acetone detection with ultralow detection limit, *Sens. Actuators, B*, 2019, **288**, 432–441.

109 M. Niu, F. Huang, L. Cui, P. Huang, Y. Yu and Y. Wang, Hydrothermal synthesis, structural characteristics, and enhanced photocatalysis of SnO_2/α-Fe_2O_3 semiconductor nanoheterostructures, *ACS Nano*, 2010, **4**, 681–688.

110 Y. Chen, C. Li, X. Ma, Q. Qiang, B. Liu, S. Cao, *et al.*, Interface defect engineering induced drastic sensing performance enhancement of $W_{18}O_{49}$@ PANI nanowires for ammonia detection at room temperature, *Appl. Surf. Sci.*, 2020, **506**, 144816.

111 L. Xu, Q. Jiang, Z. Xiao, X. Li, J. Huo, S. Wang, *et al.*, Plasma-engraved Co_3O_4 nanosheets with oxygen vacancies and high surface area for the oxygen evolution reaction, *Angew. Chem., Int. Ed. Eng.*, 2016, **128**, 5363–5367.

112 F. Han, F. Li, S. Liu and L. Niu, Sub-stoichiometric $WO_{2.9}$ as co-catalyst with platinum for formaldehyde gas sensor with high sensitivity, *Sens. Actuators, B*, 2018, **263**, 369–376.

113 D. Wang, D. Han, L. Liu and L. Niu, Sub-stoichiometric $WO_{2.9}$ for formaldehyde sensing and treatment: a first-principles study, *J. Mater. Chem. A*, 2016, **4**, 14416–14422.

114 W. Zhang, P. Xu, Y. Shen, J. Feng, Z. Liu, G. Cai, X. Yang, R. Guan, L. Su and L. Yue, Selective detection of trimethylamine utilizing nanosheets assembled hierarchical $WO_{2.9}$ nanostructure, *J. Environ. Chem. Eng.*, 2021, **9**, 106493.

115 Q. Zhang, Q. Ma, X. Wang, Y. Wang and D. Zhao, Surface double oxygen defect engineering in button-shaped porous CeO_2/$WO_{2.9}$ heterostructures for excellent *n*-butanol detection at room temperature, *Appl. Surf. Sci.*, 2023, **616**, 156536.

116 Y. Wang, D. Liu, J. Yin, Y. Shang, J. Du, Z. Kang, R. Wang, Y. Chen, D. Sun and J. Jiang, An ultrafast responsive NO_2 gas sensor based on a hydrogen-bonded organic framework material, *Chem. Commun.*, 2020, **56**, 703–706.

117 K. W. Kao, M. C. Hsu, Y. H. Chang, S. Gwo and J. A. Yeh, A sub-ppm acetone gas sensor for diabetes detection using 10 nm thick ultrathin InN FETs, *Sensors*, 2012, **12**, 7157–7168.